

1 **TC10 regulates breast cancer invasion and metastasis by**  
2 **controlling membrane type-1 matrix metalloproteinase at**  
3 **invadopodia**

4

5 Hülsemann, M.<sup>1,2</sup>, Donnelly, S.K.<sup>1</sup>, Verkhusha, P.V.<sup>1</sup>, Mao, S.P.H.<sup>1</sup>, Segall, J.E.<sup>1,2</sup>, and  
6 Hodgson, L.<sup>1,2,\*</sup>

7

8

9 <sup>1</sup> Department of Anatomy and Structural Biology, Albert Einstein College of Medicine,  
10 Bronx, NY 10461, USA.

11 <sup>2</sup> Gruss-Lipper Biophotonics Center, Albert Einstein College of Medicine, Bronx, NY  
12 10461, USA.

13

14

15

16

17

18

19 \*correspondence to:

20 Louis Hodgson: [louis.hodgson@einsteinmed.org](mailto:louis.hodgson@einsteinmed.org)

21

## 22 **Abstract**

23 During breast cancer metastasis, cancer cell invasion is driven by actin-rich protrusions  
24 called invadopodia, which mediate the extracellular matrix degradation required for the  
25 success of the invasive cascade. In this study, we demonstrated that TC10, a member  
26 of a Cdc42 subfamily of p21 small GTPases, regulates the membrane type 1 matrix  
27 metalloproteinase (MT1-MMP)-driven extracellular matrix degradation at invadopodia.  
28 We show that TC10 is required for the plasma membrane surface exposure of MT1-  
29 MMP at invadopodia. By utilizing our new Förster resonance energy transfer (FRET)  
30 biosensor, we demonstrated the p190RhoGAP-dependent regulation of spatiotemporal  
31 TC10 activity at invadopodia. We identified a pathway that regulates TC10 activity and  
32 function at invadopodia through the activation of p190RhoGAP and the downstream  
33 interacting effector Exo70 at the invadopodia sites. Our findings reveal the role of a  
34 previously unknown regulator of vesicular fusion at invadopodia, TC10, on the invasive  
35 potential of breast cancer cells during invasion and metastasis.

36

37

38

39

## 40 Introduction

41 Cancer metastasis represents a multistep process, during which cells escape from a  
42 primary tumor and disseminate throughout the body, establishing new tumors at distant  
43 sites. To achieve this dissemination, cancer cells form actin-rich protrusions called  
44 invadopodia. Mature invadopodia degrade the extracellular matrix (ECM) by recruiting  
45 membrane type 1 matrix metalloproteinases (MT1-MMP), a transmembrane protease  
46 that has been associated with ECM degradation during mammary adenocarcinoma  
47 invasion<sup>1</sup>. Invadopodia structures are spatially and temporally regulated<sup>2</sup> and are  
48 necessary to breach the basement membrane and degrade the ECM during the  
49 intra/extravasation process<sup>3-8</sup>. Although the therapeutic efficacy of proteinase inhibitors  
50 has not been successfully established in clinical applications<sup>9,10</sup>, *in vitro* and *in vivo*  
51 studies have indicated that MT1-MMP-mediated functions play important roles during  
52 the breast tumor metastatic cascade. These issues highlight our lack of clear  
53 understanding regarding the mechanisms that underlie the tumor invasion and  
54 dissemination processes, preventing the clear delineation of the contributions made by  
55 proteinase-dependent<sup>11-13</sup> and -independent<sup>14</sup> processes during tumor invasion and  
56 metastasis.

57 TC10 is a p21 small GTPase that belongs to the Rho family and is closely related to  
58 Cdc42, a canonical small GTPase. The role played by Cdc42 in the regulation of  
59 invadopodia generation has previously been demonstrated<sup>12,15</sup>. A minor paralog of  
60 Cdc42, TC10, has not yet been established as a key player in tumor invasion and  
61 metastasis<sup>16-19</sup>, although the involvement of TC10 has been recognized in other disease  
62 contexts, including diabetes<sup>20</sup>. In general, Rho-family GTPases serve as molecular  
63 switches that cycle between the GTP-bound on state and the GDP-bound off state.  
64 GTPases are regulated by guanine nucleotide exchange factors (GEFs), which  
65 exchange GDP for GTP, GTPase-activating proteins (GAPs), which induce GTP  
66 hydrolysis, and guanine nucleotide dissociation inhibitors (GDIs), which can prevent the  
67 GDP to GTP exchange. Unlike other canonical Rho GTPases, TC10 has a relatively low  
68 binding affinity for Mg<sup>2+</sup>, suggesting that wild-type (WT) TC10 may act as a fast-cycling  
69 GTPase, remaining in an activated state unless acted upon by GTPase regulators, such

70 as GAPs<sup>21,22</sup>. TC10 is highly active on exocytic vesicles and recycling endosomes, and  
71 the TC10-mediated hydrolysis of GTP is necessary to promote vesicular fusion at the  
72 plasma membrane<sup>23</sup>. TC10 interacts with Exo70 as part of a conserved, octameric  
73 exocyst complex that recruits TC10-loaded vesicles to the plasma membrane<sup>24,25</sup>. This  
74 function of TC10 is conserved in neurites<sup>26</sup>, suggesting that TC10 activity is broadly  
75 important for exocytosis. The docking of the exocyst complex at invadopodia has been  
76 observed in breast cancer cells, where it appears to control the exocytic presentation of  
77 MT1-MMP<sup>27</sup>. These observations indicate the likely involvement of a yet unknown  
78 vesicular fusion regulator that may be necessary to complete the final step of MT1-MMP  
79 surface presentation at tumor invadopodia<sup>28</sup>.

80 In this study, we showed that endogenous TC10 is localized at invadopodia and that  
81 TC10 depletion markedly reduced ECM degradation and the *in vitro* invasion of  
82 mammary adenocarcinoma cells through Matrigel-coated filters. We identified an  
83 important control node for the TC10 GTPase function involving p190RhoGAP, which is  
84 necessary for the regulation of TC10 activity at invadopodia. We observed the activation  
85 dynamics of TC10 at invadopodia using our new, sensitive, Förster resonance energy  
86 transfer (FRET)-based TC10 biosensor. Importantly, we demonstrated that the TC10-  
87 mediated hydrolysis of GTP, which is promoted by p190RhoGAP, was required for  
88 matrix degradation and the surface exposure of MT1-MMP at invadopodia. Moreover,  
89 we showed that TC10 significantly impacts breast tumor metastasis to the lungs in an *in*  
90 *vivo* mouse orthotopic model of breast cancer metastasis. Taken together, our results  
91 indicated an important role for TC10 as a regulator of exocytic vesicular control at  
92 invadopodia, involved in matrix degradation, invasion, and metastasis in breast cancer.

93

## 94 **Results**

### 95 **TC10 is localized at invadopodia and is necessary for matrix degradation**

96 TC10 is known to function in vesicular trafficking, especially during glucose receptor  
97 transport in diabetes<sup>29</sup>; however, its role in cancer has not yet been elucidated. We  
98 hypothesized that TC10 might impact cancer invasion and metastasis by regulating the  
99 functions of tumor invadopodia. We found that endogenous TC10 was localized at  
100 invadopodia in two different breast cancer cell lines: rat adenocarcinoma MTLn3 (Fig.  
101 1a) and human triple-negative MDA-MB-231 (Supplementary Fig. S1). Endogenous  
102 TC10 at invadopodia displayed two distinct localization patterns, either laterally at the  
103 sides of invadopodia or within the core of invadopodia, overlapping with the  
104 cortactin/Tks5 core marker proteins (Fig. 1b and c; Supplementary Fig. S1). Under  
105 steady-state conditions, TC10 localized predominantly to the invadopodia core (Fig. 1b).  
106 To characterize TC10 localization during the early phases of invadopodia formation, we  
107 serum-starved MTLn3 cells and then stimulated them with epidermal growth factor  
108 (EGF) to induce the synchronous formation of invadopodium precursors, which are  
109 unable yet to degrade the ECM. We found that TC10 was initially partitioned equally  
110 between the core and the regions surrounding the core, whereas 5 min after EGF  
111 stimulation, TC10 was observed to accumulate at the core (Fig. 1d). This timing relative  
112 to EGF stimulation coincided with previous observations regarding  $\beta 1$  integrin activation  
113 dynamics during EGF-stimulated invadopodia precursor formation<sup>30</sup> and with the  
114 activation of various pathways associated with this important adhesion molecule<sup>31</sup>.  
115 These observations may indicate the possible involvement of a  $\beta 1$  integrin-adhesion-  
116 mediated pathway in the modulation of TC10 activity and functions at invadopodia.

117 We next used small interfering RNA (siRNA) to deplete TC10, which resulted in reduced  
118 ECM degradation in MDA-MB-231 cells (Fig. 1e and f). A similar phenotype was  
119 observed in MTLn3 cells, which could be rescued by the overexpression of a WT TC10  
120 construct that is resistant to siRNA (Fig. 1g). The steady-state number of invadopodia  
121 was not affected by TC10 depletion (Fig. 1h), indicating a limited role for TC10 in the  
122 structural aspects of invadopodia regulation. Corroborating this observation, the

123 lifetimes (turnover rates) of invadopodia were not significantly impacted by TC10  
124 depletion (Fig. 1i). To explore the functional role of TC10 on its effects on matrix  
125 degradation, we overexpressed a TC10-Q75L mutant<sup>23</sup>, which lacks the catalytic ability  
126 to hydrolyze GTP. The overexpression of TC10-Q75L resulted in an ECM degradation  
127 defect similar to that observed under TC10 depletion conditions (Fig. 1k), and no effect  
128 on the total number of invadopodia was observed (Fig. 1l). Together, these  
129 observations indicated that the ability of TC10 to hydrolyze GTP and its GTPase cycling  
130 activity are necessary to regulate the ECM degradation function of invadopodia. These  
131 results also suggested that TC10 plays a functional role, rather than a structural role,  
132 during invadopodia dynamics and tumor invasion.

### 133 **TC10 regulates MT1-MMP exposure at the plasma membrane of invadopodia**

134 Because TC10 plays a well-known role in vesicular trafficking<sup>23</sup>, in addition to the  
135 impacts on ECM degradation at invadopodia observed in the previous experiment, we  
136 hypothesized that TC10 regulates the MT1-MMP surface presentation at invadopodia  
137 by controlling vesicular fusion at the plasma membrane during exocytosis. To test this  
138 hypothesis, we first examined the endogenous localization of MT1-MMP at invadopodia  
139 and found two distinct patterns of localization: within the invadopodia core and laterally  
140 flanking the invadopodia core (Fig. 2a), with the side localization being more  
141 predominant (Fig. 2b). We then overexpressed an MT1-MMP with an enhanced green  
142 fluorescent protein (EGFP) tag on the C-terminal, cytoplasmic end. We overexpressed  
143 this EGFP-tagged MT1-MMP construct in MTLn3 cells and antibody stained the  
144 surface-exposed MT1-MMP without permeabilizing the plasma membrane. When TC10  
145 was depleted in these cells, we observed a significant reduction in the proportion of  
146 surface-exposed MT1-MMP staining relative to the total MT1-MMP level, as measured  
147 by tracking the EGFP fluorescence intensity (Fig. 2c). No difference in total MT1-MMP  
148 levels at invadopodia was observed between the control and TC10-depleted cells (Fig.  
149 2c). These observations suggested that TC10 plays an important role in the surface  
150 exposure of MT1-MMP at the plasma membrane, without affecting the trafficking of  
151 MT1-MMP-containing vesicles or the loading of MT1-MMP cargo onto vesicles.

152 Previously, the exocyst complex was observed to dock onto the lateral aspect of  
153 invadopodia, which was shown to be important for ECM degradation by invadopodia in  
154 breast cancer invasion<sup>32</sup>. Exo70 is a component of the octameric exocyst complex,  
155 which plays a critical role in vesicular docking at the cell membrane and is essential for  
156 the exocytic secretion of MMP at invadopodia<sup>33</sup>. Because TC10 has been shown to  
157 interact with Exo70<sup>34</sup>, we examined the role played by the TC10–Exo70 interaction on  
158 MT1-MMP surface exposure and ECM degradation. We found that Exo70 localization  
159 strongly overlapped with TC10, both within the invadopodia core and at the lateral  
160 aspects of invadopodia (Fig. 2d). Unlike the MT1-MMP localization, however, Exo70  
161 was predominantly localized with TC10 in the invadopodia core (Fig. 2e).  
162 P29L/E31V/Y32H mutations in the switch I/II regions of Cdc42, which are important for  
163 effector interactions, have been shown previously to disrupt Cdc42–Exo70 co-  
164 immunoprecipitation<sup>35,36</sup>. When analogous mutations (P43L/E45V/Y46H) were  
165 introduced into TC10, we observed only a modest reduction in the co-  
166 immunoprecipitation of Exo70 with TC10 (Lane 6: Fig. 2f). When two additional effector  
167 binding mutations were introduced (T49A and Y54C, which are analogous to mutations  
168 in Cdc42 that impact activity status and effector interactions)<sup>37</sup>, a further reduction in co-  
169 immunoprecipitation was observed (Lane 7: Fig. 2f), suggesting that these additional  
170 mutations further interfered with complex formation. Although the constitutively active,  
171 GTP-hydrolysis-deficient version of TC10 (Q75L) only modestly immunoprecipitated  
172 with Exo70, similar to the dominant-negative T31N TC10 mutant (Lanes 4 and 5: Fig.  
173 2f), the F42L mutation, which is analogous to a mutation that renders other  
174 RhoGTPases into fast-cycling GTPases, resulted in the strong immunoprecipitation of  
175 Exo70 (Lane 3: Fig. 2f). These results suggested that GTP hydrolysis and nucleotide  
176 cycling activity is important for efficient TC10–Exo70 complex interactions and that  
177 mutating the residues P43L/E45V/Y46H/T49A/Y54C (“5×-mutation”) within the Switch  
178 I/II region of TC10 was able to impact this interaction. We then used this 5×-mutated  
179 TC10, co-expressed with Exo70 in MTLn3 cells, and observed a significant impact on  
180 the ability of these cells to degrade the ECM (Fig. 2g), without affecting the total number  
181 of steady-state invadopodia (Fig. 2h). The expression of the 5×-mutated version of  
182 TC10 altered the localization pattern of Exo70 at invadopodia (Fig. 2i) but did not alter

183 the TC10 localization pattern in invadopodia (Supplementary Fig. S4b). These  
184 observations indicated that the TC10-Exo70 interaction is important for the appropriate  
185 targeting of Exo70 within invadopodia and that this interaction impacts ECM  
186 degradation. Furthermore, these results indicated a potential mechanism through which  
187 MT1-MMP might be deposited into the plasma membrane, as MT1-MMP-loaded  
188 vesicles containing TC10 approach the lateral/side aspect of invadopodia. GTP  
189 hydrolysis by vesicular-bound TC10 may begin to occur in this region, where TC10  
190 might first encounter a cognate GAP that resides within the invadopodium core, which  
191 facilitates GTP hydrolysis by TC10 to promote the plasma membrane fusion of the  
192 vesicles.

### 193 **TC10 activity at invadopodia is spatially regulated**

194 Because GTP hydrolysis is necessary for TC10-mediated vesicular fusion at the plasma  
195 membrane<sup>23</sup>, we evaluated the activation dynamics of TC10 at and surrounding the  
196 invadopodia. For this purpose, we designed a new FRET-based TC10 biosensor (Fig.  
197 3a). The biosensor design is based on a monomeric, single-chain, genetically encoded  
198 approach that is TC10-specific, similar to the design of our previous Rac and Cdc42  
199 sensors<sup>38,39</sup>. The biosensor consists of a monomeric Cerulean 1 and monomeric  
200 circularly permuted (cp229) Venus fluorescent protein FRET pair with an optimized  
201 Rac/Cdc42-binder motif from our Rac/Cdc42 biosensors<sup>38,40-42</sup>, and full-length TC10  
202 (Fig. 3a). The spectrofluorometric characterization of the TC10 FRET biosensor  
203 revealed an approximately 80% difference in FRET/donor emission ratio between the  
204 constitutively activated (Q75L) and off states (the dominant-negative T31N or other  
205 effector binding mutants) of the TC10 biosensor (Fig. 3b). The WT TC10 version of the  
206 biosensor showed high FRET, similar to two different constitutively active TC10  
207 biosensor mutants (G26V and Q75L, Fig. 3c), corroborating previous reports that WT  
208 TC10 represents an activated GTPase due to a low Mg<sup>2+</sup>-binding affinity<sup>23</sup>. The co-  
209 expression of Rho-targeting p50RhoGAP and p190RhoGAP but not Rap-targeting  
210 Rap1GAP1 resulted in the attenuation of FRET (Fig. 3d). The co-expression of  
211 caveolin1, a putative GDI for TC10<sup>29</sup>, resulted in attenuation of FRET (Supplementary  
212 Fig. S5a). To confirm that the expression of the TC10 biosensor did not result in

213 aberrant overexpression artifacts in downstream signaling, we performed a competitive  
214 pull-down assay using purified, exogenous binding domain. The activated TC10  
215 biosensor only interacted with an exogenous effector when both biosensor binding  
216 domains within the biosensor were mutated (2XPBD: H83/86D), preventing an  
217 interaction between activated TC10 and the GTPase binder motif within the biosensor  
218 backbone (Supplementary Fig. S5b). When the TC10 biosensor was overexpressed in  
219 MTLn3 breast cancer cells, we observed an approximately 30% difference in whole-cell  
220 average TC10 activities between the constitutively active and dominant-negative  
221 versions of the TC10 biosensor (Supplementary Fig. S5c). The biosensor also  
222 responded to stimulation with serum and EGF following serum starvation  
223 (Supplementary Fig. S5d). We then applied a synonymous codon modification<sup>43</sup>, which  
224 prevents homologous recombination during transfection and transduction into tumor  
225 cells. The TC10 biosensor was stably transduced and integrated into tet-OFF tTA-  
226 MTLn3 cells<sup>44</sup>, under the control of a tet-inducible promoter, to achieve tight expression  
227 control.

228 Using the new TC10 FRET biosensor, we attempted to determine the dynamics of TC10  
229 activity at and surrounding the invadopodia. We co-transduced cortactin-miRFP703 to  
230 serve as a marker of the invadopodia core and observed TC10 activity. The biosensor  
231 activities at invadopodia appeared to be highly dynamic and fluctuated markedly during  
232 live-cell imaging (Fig. 3e), indicating stochastic behavior over time. We first reduced the  
233 complexity of the data temporally by integrating the TC10 activities over time in steady-  
234 state invadopodia, similar to a previous analysis performed for a different class of Rho  
235 GTPase<sup>39</sup>. We measured and averaged the line scans across invadopodia and  
236 determined that the center of the invadopodium core showed a significant reduction in  
237 time-integrated TC10 activity compared with the regions surrounding the invadopodium  
238 core (Fig. 3f), which suggested the apparent stochastic fluctuation of TC10 activity at  
239 invadopodia, underlying spatially ordered distribution of TC10 activity. A similar  
240 observation was made in MDA-MB 231 cells (Supplementary Fig. S7). To further  
241 quantify the TC10 activity fluctuation, we defined two regions by generating a binary  
242 mask, with one region based on the cortactin core (“core”) and the second region  
243 defined by dilating the core mask by 30 pixels and subtracting the core to form an

244 annulus (“ring”). The live-cell biosensor measurements were analyzed by  
245 autocorrelation to extract the characteristic periodicity<sup>38,45,46</sup> at these two regions. We  
246 observed no periodic fluctuations in TC10 activity for either region, as characterized by  
247 the lack of repeated, oscillatory crossings of the zero axis in the autocorrelation  
248 functions (Fig. 3g), which indicated that the TC10 activity dynamics in WT, steady-state  
249 invadopodia are stochastic in nature. Importantly, the time-integrated activity of TC10 is  
250 attenuated significantly in the core, indicating a potential mechanism through which a  
251 core-localized GAP may regulate TC10 GTP-hydrolysis activity at the invadopodia core  
252 (Fig. 3f).

### 253 **p190RhoGAP impacts invadopodia function by targeting TC10**

254 To identify the regulator of TC10 function at invadopodia, we focused on p190RhoGAP  
255 (*Arhgap35*), a well-known, integrin-adhesion-associated regulator of RhoGTPases,  
256 which binds cortactin within the invadopodia core during invadopodia precursor  
257 formation and is present within the core of invadopodia at steady state<sup>7</sup>. Traditionally,  
258 p190RhoGAP targets Rac and Rho GTPase isoforms and contains: an N-terminal  
259 GTPase-binding domain; four FF domains involved in binding transcription factors; a  
260 protrusion localization domain that binds cellular cortactin or Rnd3 GTPase; a  
261 p120RasGAP binding site; a polybasic region; and a C-terminal consensus GAP  
262 domain that can switch specificity between Rac-GTP and Rho-GTP<sup>47,48</sup>. p190RhoGAP  
263 has been associated with the regulation of TC10 activity in a number of systems,  
264 including the leading edge of HeLa cells and neurite extensions<sup>23,49</sup>. In melanoma,  
265 tyrosine phosphorylation and the activation of p190RhoGAP at invadopodia in response  
266 to laminin peptide depends on the activation of  $\beta 1$  integrins<sup>50</sup>; in breast cancer,  
267 invadopodia precursor  $\beta 1$  integrins are activated within 3 to 5 min after EGF stimulation  
268 in a Rac3 GTPase-dependent manner<sup>30,38</sup>.  $\beta 1$  integrin recruits the non-receptor tyrosine  
269 kinase Arg (Ableson-related gene, also known as Abl2) and stimulates the Arg-  
270 dependent phosphorylation of p190RhoGAP at the leading edge of fibroblasts; however,  
271 whether this occurs in breast cancer cell invadopodia has not yet been elucidated.

272 Steady-state and EGF-stimulated invadopodia precursor assays demonstrated that  
273 p190RhoGAP is a resident protein of the invadopodia core (Fig. 4a and b), and  
274 p190RhoGAP depletion phenocopied the ECM degradation deficiency observed with  
275 TC10 depletion (Fig. 4c and Supplementary Fig. S9a and b). The overexpression of a  
276 dominant-negative version of p190RhoGAP, which lacks the ability to activate GTP  
277 hydrolysis by Rho GTPases, also strongly inhibited ECM degradation (Fig. 4c).  
278 Moreover, invadopodia lifetimes were not impacted by p190RhoGAP depletion (Fig. 4d),  
279 which suggested that p190RhoGAP is associated with the functional aspects of  
280 invadopodia, rather than the structural aspects, similar to TC10. p190RhoGAP depletion  
281 was associated with a reduction in the TC10 proportion observed in the invadopodia  
282 core, accompanied by an increase in the proportion of TC10 observed in the lateral  
283 aspects of invadopodia (Fig. 4e), which suggested that the flux of TC10 through the  
284 ring-like region and into the invadopodia core was significantly attenuated by  
285 p190RhoGAP depletion. In line with our hypothesis that TC10 activity might be affected  
286 by perturbations in p190RhoGAP activity, p190RhoGAP depletion also impacted the  
287 surface presentation of MT1-MMP in a manner similar to that observed for TC10  
288 depletion (Fig. 4f). These findings indicated that p190RhoGAP plays an important role in  
289 the regulation of invasive functions associated with invadopodia.

290 Next, we attempted to determine the functional impacts of p190RhoGAP on TC10  
291 activity at invadopodia. We used our FRET biosensor to monitor changes in TC10  
292 activity following p190RhoGAP depletion at invadopodia. Live-cell imaging of TC10  
293 activity in p190RhoGAP-depleted cells revealed strong fluctuations in the activity  
294 patterns at and surrounding the invadopodia (Fig. 4g). We integrated the TC10 activity  
295 over time at invadopodia and performed a line scan analysis, which showed that the  
296 time-integrated activity of TC10 was significantly elevated within the invadopodia core in  
297 cells with p190RhoGAP depletion (Fig. 4h). To characterize the temporal fluctuations of  
298 TC10 activity at invadopodia under p190RhoGAP depletion conditions, we used the  
299 autocorrelation analysis. We found that the core-associated TC10 activity dynamics  
300 were stochastic and lacked periodicity, similar to WT conditions (Figs. 4i and 3g).  
301 Interestingly, we found that p190RhoGAP depletion produced a small periodic  
302 oscillation in TC10 activity in the ring-like region surrounding the core (Fig. 4i). The

303 characteristic periodicity observed for the TC10 activity fluctuation in the ring-like region  
304 of invadopodia was approximately 5 min, which is within a similar order of magnitude as  
305 previously determined invadopodium core protein fluctuation rates, including those for  
306 cortactin and neural Wiskott-Aldrich syndrome protein (N-WASP)<sup>36</sup>. These observations  
307 suggest the transient, bulk flux of TC10 activity through the ring-like region surrounding  
308 the invadopodia core in the absence of GTP hydrolysis under p190RhoGAP depleted  
309 conditions. This may reduce the degree of freedom of activity modulation and could  
310 produce a periodic function characterizing only the bulk flux of active TC10 through the  
311 ring-like region in transit into the core (Supplementary Fig. S9c). The absolute value of  
312 the fluctuation amplitude was significantly reduced in the ring-like region compared with  
313 that in the core when p190RhoGAP was depleted (Fig. 4j), supporting the hypothesis  
314 that p190RhoGAP depletion resulted in reduced degrees of freedom. This observation  
315 is consistent with the hypothesis that p190RhoGAP regulates the ability of TC10 to  
316 hydrolyze GTP as it transits from the ring-like region into the invadopodia core, where  
317 p190RhoGAP primarily resides.

318 In addition to targeting TC10, RhoC GTPase activity is also directly impacted by  
319 p190RhoGAP<sup>35,39,51</sup>. Previously, the inactivation of RhoC was shown to increase ECM  
320 degradation at invadopodia via a mechanism associated with changes to the  
321 invadopodia structural cohesion through the RhoC-Rho kinase 1 (ROCK)-LIM kinase  
322 (LimK)-cofilin-phosphorylation pathway<sup>39</sup>. p190RhoGAP depletion would, therefore, be  
323 expected to cause the overactivation of RhoC<sup>51</sup>. We generated a fast-cycling,  
324 constitutively activated RhoC (F30L) that contained a set of analogous GAP-binding  
325 deficiency mutations (E93H and N94H)<sup>52</sup>. The overexpression of this mutant RhoC  
326 would allow the effects of p190RhoGAP depletion to be mimicked for RhoC without  
327 affecting the ability of native p190RhoGAP to target TC10. The overexpression of this  
328 RhoC mutant impacted ECM degradation but had no significant effects on the total  
329 number of steady-state invadopodia or the relative MT1-MMP localization at  
330 invadopodia (Supplementary Fig. S10). However, as expected, based on the structural  
331 effects of RhoC on invadopodia, we observed a shift in the invadopodia lifetimes,  
332 favoring structures with faster turnover rates and reducing those with longer lifetimes  
333 (Supplementary Fig. S10). An increase in the population of invadopodia that turnover

334 rapidly is associated with structural instability, which impacts invadopodia maturation  
335 and reduces ECM degradation. Thus, RhoC activation affects ECM degradation, likely  
336 through structural effects rather than vesicular targeting or fusion defects. These  
337 observations indicate the divergent roles of TC10- and RhoC-driven pathways at  
338 invadopodia that are simultaneously regulated by a single upstream regulator  
339 p190RhoGAP.

340 **Tyrosine phosphorylation of p190RhoGAP is required for ECM degradation**

341 The phosphorylation of p190RhoGAP by the non-receptor tyrosine kinase Arg promotes  
342 the binding of p190RhoGAP to p120RasGAP and initiates the recruitment of the  
343 p190:120 complex to the cell periphery, where the GAP activity of p190RhoGAP for  
344 RhoGTPases is potentiated<sup>53,54</sup>. Arg is activated by  $\beta 1$  integrin binding during  
345 invadopodia maturation<sup>30</sup>. Arg phosphorylates p190RhoGAP at Y1105, in the RasGAP-  
346 binding region, and Y1087, which stabilizes the interaction between p190RhoGAP and  
347 p120RasGAP<sup>53</sup>. Therefore, we determined the phosphorylation status at Y1105 of  
348 p190RhoGAP at invadopodia and examined how phosphorylation activity affected the  
349 p190RhoGAP-mediated regulation of invadopodia functions. Approximately 90% of  
350 steady-state invadopodia contained Y1105-phosphorylated p190RhoGAP, which was  
351 found both in the core compartment and occasionally on the lateral sides of invadopodia  
352 (Fig. 5a and b), which agrees with a previous study that showed that only the active,  
353 phosphorylated form of p190RhoGAP was recruited to the plasma membrane to act on  
354 RhoGTPases<sup>53,54</sup>. The phosphorylation of p190RhoGAP at Y1105 is time-dependent  
355 following EGF stimulation to induce the synchronous formation of invadopodia  
356 precursors (Fig. 5c), mirroring the previously described Arg-mediated phosphorylation  
357 events at the invadopodium core following EGF stimulation<sup>55</sup>. In line with the tyrosine-  
358 phosphorylated status of p190RhoGAP, we observed a strong colocalization between  
359 p120RasGAP, p190RhoGAP, and TC10 at invadopodia, either on the side of the  
360 invadopodia or in the core, overlapping with the cortactin signal (Fig. 5d and e). The  
361 colocalization of p190RhoGAP at the invadopodia core was significantly altered by the  
362 expression of a competitive inhibitor of p190:120 binding<sup>53,54</sup>, shifting to a lateral  
363 localization pattern (Fig. 5f). The presence of this competitive inhibitor also reduced

364 ECM degradation (Fig. 5g) without impacting the number of steady-state invadopodia  
365 (Fig. 5h). Phosphorylation-deficient p190RhoGAP point mutations, in which the two  
366 phosphorylated tyrosines were replaced with phenylalanines (Y1105F and Y1087F),  
367 strongly impacted ECM degradation, similar to the effects observed in response to  
368 TC10 and p190RhoGAP depletion and the overexpression of the p190:120 competitive  
369 binding inhibitor (Fig. 5i). However, these p190RhoGAP point mutations only affected  
370 the functional aspects of invadopodia without affecting the number of steady-state  
371 invadopodia (Fig. 5j). These observations indicated that p190RhoGAP is targeted to the  
372 invadopodia core through tyrosine phosphorylation, which promoted p120RasGAP  
373 binding.

374 **TC10 is required for cancer cell metastasis *in vivo***

375 We attempted to determine the functional relevance of TC10 signaling for the process of  
376 breast cancer cell invasion and metastasis. We first investigated the ability of tumor  
377 cells to invade through the ECM using an *in vitro* invasion assay, in which cultured  
378 tumor cells respond to serum stimulation by migrating through a Matrigel-coated filter<sup>28</sup>.  
379 Compared with the control siRNA-treated condition, TC10 depletion significantly  
380 impacted the ability of MTLn3 cells to invade through Matrigel-coated filters in an *in vitro*  
381 invasion assay (Fig. 6a), which was expected due to the reduced ECM degradation  
382 capacity and the reduced MT1-MMP presentation at invadopodia. Moreover,  
383 p190RhoGAP depletion in MTLn3 cells also significantly attenuated the ability of these  
384 cells to invade, phenocopying TC10 depletion (Fig. 6b). To examine whether TC10 is  
385 required for breast tumor metastasis in a mouse model, we generated a clustered  
386 regularly interspaced short palindromic repeat (CRISPR)/CRISPR-associated 9 (Cas9)-  
387 driven TC10 knockout cell line in MTLn3 cells that stably express EGFP. We chose the  
388 CRISPR/Cas9 knockout cell population expressing single-guide RNA (sgRNA) #4,  
389 which showed the strongest TC10 knockout efficiency in a stable cell population (Fig.  
390 6c). TC10 knockout cells showed significant ECM degradation defects (Fig. 6d) but no  
391 changes in the total number of steady-state invadopodia, similar to the effects observed  
392 for siRNA-mediated TC10 depletion (Fig. 6e). ECM degradation deficiencies in the  
393 TC10 knockout cells could be fully rescued by the overexpression of WT TC10 (Fig. 6f).

394 We orthotopically injected TC10 knockout cells into the mammary fat pads of 6-8-week-  
395 old female severe combined immunodeficient (SCID) mice and examined lung  
396 metastasis after the primary tumor reached 1 cm in diameter. Lung metastasis was  
397 significantly impacted in mice bearing TC10-knockout MTLn3 tumors compared with  
398 mice bearing non-targeting control tumors (Fig. 6g). Together, these results suggest  
399 that TC10 functionally impacts breast tumor dissemination and metastasis.

400

## 401 Discussion

402 In this study, we demonstrated a new role for TC10 GTPase, a close paralog of Cdc42,  
403 in breast cancer invasion and metastasis at breast tumor invadopodia. We designed  
404 these studies to test our hypothesis that an important, previously unidentified GTPase,  
405 might regulate the invadopodia surface presentation of MT1-MMP enzymes, which are  
406 necessary for ECM degradation during tumor invasion. Our results suggested a model  
407 in which TC10 regulates MT1-MMP-containing vesicular fusion at the invadopodia  
408 membrane, which is influenced by the regulation of activity of TC10 by the upstream  
409 regulator p190RhoGAP (*Arhgap35*) at invadopodia (Fig. 6h). Our findings indicated that  
410 TC10, an important member of the Cdc42-class of Rho GTPases, plays an important  
411 role during breast cancer invasion and metastasis through the control of ECM  
412 degradative functions at invadopodia structures.

413 TC10 depletion resulted in significant impacts on the ability of tumor cells to degrade the  
414 ECM, associated with a decrease in the surface exposure of MT1-MMP at invadopodia.  
415 Because the overall number of steady-state invadopodia and invadopodia lifetimes were  
416 not significantly impacted by TC10 perturbations, TC10 appears to primarily play a  
417 functional role at invadopodia, without being involved in the structural aspects of  
418 invadopodia maintenance. This finding is in stark contrast with the role played by the  
419 canonical GTPase, Cdc42, at invadopodia, as the activation of Cdc42 by an upstream  
420 GEF, Vav1, has been shown to be critical for the initial formation of invadopodia  
421 precursors<sup>56,57</sup>. We also observed the transient but persistent activation of Cdc42 within  
422 the nascent core of invadopodia precursor structures during the assembly of the  
423 cortactin core (Supplementary Fig. S11). Our observations indicated that these close  
424 paralog GTPases play divergent roles at invadopodia structures during invadopodia  
425 assembly and function.

426 p190RhoGAP has been documented to primarily target Rac and Rho GTPases<sup>58</sup>. We  
427 previously localized p190RhoGAP at both the leading edge and the core of invadopodia  
428 in breast cancer cells<sup>39,51</sup>, likely due to binding with cortactin via its protrusion  
429 localization domain<sup>43</sup>. In these previous studies, we showed that p190RhoGAP targeted

430 another class of RhoGTPase, RhoC, to impact actin polymerization both at the leading  
431 edge and within the core of invadopodia<sup>39,51</sup>. In our present work, we showed that  
432 p190RhoGAP also targets TC10 at invadopodia to regulate TC10 activity, which  
433 ultimately affects the surface presentation of MT1-MMP and ECM degradation.  
434 Moreover, we previously showed that Rac1 activity was attenuated within the  
435 invadopodia core and that the subsequent activation of Rac1 was critical for the  
436 regulation of invadopodia structural turnover<sup>41</sup>. Although we did not identify a specific  
437 GAP involved in Rac1 regulation in that study, the over-activation of Rac1 reduced the  
438 total number of invadopodia, whereas the depletion of p190RhoGAP in the present  
439 study did not change the total number of steady-state invadopodia or affect invadopodia  
440 lifetimes compared with control conditions. These observations suggest that a different  
441 set of signaling pathways are likely responsible for regulating Rac1 activity at  
442 invadopodia, separate from the p190RhoGAP-TC10 pathway. RhoGAPs have been  
443 shown to be relatively promiscuous, interacting with many GTPases<sup>59</sup>; therefore, the  
444 multi-specificity of p190RhoGAP at invadopodia is likely to coordinate the signaling  
445 regulation of a number of RhoGTPases, including RhoC and TC10 but not Rac1.

446 Interestingly, the depletion of p190RhoGAP led to an accumulation of TC10 at the  
447 lateral side of invadopodia, while the fraction of TC10 occupying the core of invadopodia  
448 was significantly reduced. This observation suggests that the flux of TC10-containing  
449 vesicles into the invadopodia core region could be impacted when p190RhoGAP is  
450 depleted. Corroborating this observation, a complete shutdown of vesicular flux has  
451 been previously observed when another GTPase important for the regulation of vesicular  
452 trafficking, (Arf6) was perturbed<sup>38,60</sup>. Here, the GTP-hydrolysis by TC10 was perturbed  
453 through the depletion of p190RhoGAP. This perturbation of p190-TC10 signaling node  
454 likely prevented the exocytic fusion of the vesicles at the plasma membrane of  
455 invadopodia core and significantly attenuated the flux of the vesicles containing TC10  
456 into the invadopodia core compartment. Importantly, those TC10 that were still able to  
457 transport into the invadopodia core compartment when p190RhoGAP was depleted,  
458 showed significantly elevated activity, pointing to the lack of p190RhoGAP-action on  
459 that population of TC10.

460 During the p190RhoGAP activation cascade<sup>61</sup>, the non-receptor tyrosine kinase Arg  
461 phosphorylates p190RhoGAP tyrosines 1105 and 1087<sup>53</sup>. The phosphorylation of these  
462 two sites is dependent on  $\beta 1$  integrin activation and is important for the formation of a  
463 complex between p190RhoGAP and p120RasGAP, which promotes the appropriate  
464 localization and GAP activity of p190RhoGAP toward RhoGTPases during cell  
465 adhesion<sup>53,62,63</sup>. In the present study, we showed that the phosphorylation of Y1105 is  
466 time-dependent following EGF stimulation and mirrors the previously reported Arg-  
467 mediated phosphorylation dynamics at the invadopodia core following EGF  
468 stimulation<sup>64</sup>. Furthermore, the expression of a phosphorylation-deficient p190RhoGAP  
469 mutant strongly impacted ECM degradation. The expression of a competitive inhibitor,  
470 based on the SH2-SH3-SH2 motif sequence in p120RasGAP, which is important for  
471 binding to phospho-tyrosine 1105 in p190RhoGAP<sup>53,54</sup>, significantly impacted both ECM  
472 degradation and the localization of p190RhoGAP at the invadopodia core. In line with  
473 the important role played by p120RasGAP binding on the control of p190RhoGAP  
474 localization and function, p120RasGAP depletion also resulted in reduced ECM  
475 degradation by invadopodia (Supplementary Fig. S12). However, we also noted a small  
476 but significant reduction in the total number of invadopodia when p120RasGAP was  
477 depleted (Supplementary Fig. S12). This observation may indicate that p120RasGAP  
478 might also play a role in invadopodia assembly or the maintenance of structural  
479 components, possibly associated with its documented role during  $\beta 1/2$  integrin  
480 recycling<sup>65</sup>. Changes in integrin recycling mechanisms could alter the availability of  
481 functional integrins at the cell surface, which could potentially impact invadopodia  
482 stability and turnover. Our findings indicated the importance of the localization and  
483 functional mechanisms of the p190:p120 GAP-signaling complex at the invadopodia  
484 core, which target GTPases, including TC10, to regulate invadopodia functions.

485 The functional consequences of TC10 activity regulation and the associated effects on  
486 ECM degradation, cell invasion, and metastasis were underscored by our findings from  
487 the *in vitro* invasion and *in vivo* metastasis assays. Although the initial growth rates of  
488 primary tumors seeded using CRISPR/Cas9 TC10-knockout MTLn3 cells were similar  
489 to primary tumors seeded using non-targeting control cells (data not shown), metastasis

490 was significantly reduced. Given the reduced invasion caused by TC10 loss, we  
491 speculate that TC10 depletion resulted in strong impacts during vascular-crossing or on  
492 secondary metastatic outgrowths. A full analysis of the *in vivo* effects of TC10 loss on  
493 metastatic capability is beyond the scope of this work, but our studies suggest TC10  
494 plays a critical role in facilitating the efficient metastatic spread of breast tumor cells  
495 within the metastatic cascade via targeting of MT1-MMP surface exposure at  
496 invadopodia.

497

498

## 499 **Acknowledgment**

500 This work was supported by an American Cancer Society Lee National Denim Day  
501 Postdoctoral Fellowship [PF-15-135-01-CSM (S.D.)]; NIH grants [CA100324 (J.E.S.),  
502 T32GM007288 (S.P.H.M.), and R35GM136226 (L.H.)]. J.E.S. is the Betty and Sheldon  
503 Feinberg Senior Faculty Scholar in Cancer Research. L.H. is a Hirschl Career Scientist.  
504 We thank members of the Condeelis, Segall, and Cox laboratories at Albert Einstein  
505 College of Medicine for their helpful discussions.

## 506 **Author contributions**

507 M.H., S.K.D., and L.H. conceived the project. M.H. and L.H. designed experiments.  
508 M.H., S.K.D., and L.H. performed experiments. M.H. and L.H. analyzed the results.  
509 P.V.V. and L.H. designed the biosensors and characterized the biosensors. S.P.H.M.,  
510 J.E.S., and L.H. performed the metastasis assay. L.H. directed the project. M.H. and  
511 L.H. wrote and revised the manuscript. All authors reviewed the manuscript and  
512 provided feedback.

## 513 **Competing interest statement**

514 The authors declare no competing financial interests.

## 515 **Methods**

### 516 **Cell Culture**

517 MTLn3 cells (rat adenocarcinoma)<sup>66</sup> were cultured in Minimum Essential Medium  
518 (MEM, Corning, Corning, NY, USA) supplemented with 5% fetal bovine serum (FBS),  
519 1% glutamine, and 100 I.U. penicillin and 100 µg/mL streptomycin (Invitrogen, Carlsbad,  
520 CA, USA), as previously described<sup>67</sup>. MDA-MB-231 (HTB-26, ATCC, Manassas, VA,  
521 USA) cells were cultured in Dulbecco's modified Eagle medium (DMEM, Corning)  
522 supplemented with 10% FBS, 1% glutamine, and penicillin/streptomycin, as previously  
523 described<sup>38</sup>. All cell lines were tested regularly for mycoplasma using the PCR-based  
524 assay (Stratagene, San Diego, CA, USA).

### 525 **Transfection**

526 Plasmid transfections were performed in OptiMEM, using Lipofectamine 2000  
527 (Invitrogen). Cells were plated at  $1 \times 10^5$  cells/well in a 6-well plate and incubated  
528 overnight prior to transfection. Following the manufacturer's protocols, 2 µg of total DNA  
529 was transfected into each well of a 6-well plate. Cells were treated with the transfection  
530 mixture for 45 min, and the transfection was terminated by exchanging the medium with  
531 the normal growth medium.

### 532 **ECM Degradation assay**

533 Alexa Fluor 405 NHS Ester (Thermo Fisher Scientific, Waltham, MA, USA) was  
534 conjugated with 0.2% porcine gelatin (Sigma-Aldrich, St. Louis, MO, USA), according to  
535 the Thermo Fisher bioconjugation protocol. Glass coverslips (25 mm, circular #1.5,  
536 Warner Instruments, Hamden, CT, USA) were coated with 0.01% poly-L-lysine for 20  
537 min at room temperature (RT), followed by a 15 min treatment with 0.2% glutaraldehyde  
538 in phosphate-buffered saline (PBS). The Alexa Fluor 405-labeled gelatin aliquot was  
539 centrifuged at 22,000 rcf for 10 min at RT to pellet any precipitates, the supernatant  
540 was diluted 1:4 with unlabeled 0.2% gelatin, and maintained at 37°C. The  
541 glutaraldehyde-treated coverslips were coated with the Alexa 405-gelatin mixture for 10

542 min at RT, followed by a 5 min treatment with 0.2% glutaraldehyde. Then, the coverslips  
543 were incubated in 5 mg/mL NaBH4 solution for 15 min at RT and washed 3 × with PBS.  
544 The coverslips were placed in normal culture media at 37°C and 5% CO<sub>2</sub> for at least 20  
545 mins prior to cell plating. Cells were plated at a density of 1.5 × 10<sup>5</sup> cells/coverslip in  
546 wells of a 6-well plate for 16 h before fixation with 1% paraformaldehyde (PFA) for 15  
547 mins at RT. ECM degradation was measured by quantifying the mean area of non-  
548 fluorescent pixels per field, using a manual threshold in MetaMorph software (ver.  
549 7.10.3; Molecular Devices, San Jose, CA, USA). For experiments in which a transgene  
550 was expressed in cells, only the degraded areas under the transfected cells, as  
551 identified by fluorescent protein expression, were considered.

552 **EGF stimulation**

553 EGF stimulation was performed as previously described<sup>39,41</sup>. In brief, MTLn3 cells were  
554 starved for 4 h in L15 media containing 0.003% bovine serum albumin (BSA) at 37°C,  
555 without CO<sub>2</sub>, and then stimulated with 5 nM EGF (Invitrogen) for the indicated times at  
556 37°C before fixation for 15 min at RT using 1% PFA.

557 **Western Blotting**

558 Cells were lysed on ice in a buffer containing 1% NP-40, 50 mM Tris pH 7.4, 150 mM  
559 NaCl, 10 mM ethylenediaminetetraacetic acid (EDTA), 1 mM phenylmethylsulfonyl  
560 fluoride (PMSF), and 1× protease inhibitor cocktail (Sigma). The lysate was clarified by  
561 centrifugation at 22,000 rcf for 10 min at 4°C. Lysates were resolved by 8%–12%  
562 sodium dodecyl sulfate-polyacrylamide gel electrophoresis (SDS-PAGE). Proteins were  
563 transferred to polyvinylidene fluoride membranes. After blocking for at least 1 hour in  
564 5% BSA in Tris-buffered saline containing Tween-20 (TBS-T), membranes were  
565 incubated with primary antibodies at 1:1000 dilution overnight at 4°C. Membranes were  
566 incubated with secondary fluorescently labeled antibodies (LI-COR Biosciences,  
567 Lincoln, NE, USA) at 1:10,000 dilution for 1 h at RT. Immunoblots were visualized using  
568 the Odyssey Imager (LI-COR Biosciences).

569 **Antibodies**

570 TC10 (Novus, Littleton, CO, USA; 07-2151; rabbit polyclonal used at 1:500 for western  
571 blots), p190 (BD Transduction Laboratories; 610149; Clone 30/p190; mouse  
572 monoclonal), p120 (Abcam, Cambridge, UK; ab2922; Clone B4F8; mouse monoclonal),  
573 Exo70 (Santa Cruz Biotechnology; sc-365825; Clone D-6; mouse monoclonal), Vamp7  
574 (Abcam; ab36195; Clone 158.2; mouse monoclonal), MT1-MMP-Hinge region (Millipore,  
575 Burlington, MA, USA; AB6004; rabbit polyclonal), MT1-MMP (Millipore; MAB3328;  
576 Clone LEM-2/15.8; mouse monoclonal), MT1-MMP (Abcam; ab38971; rabbit  
577 polyclonal), Cortactin (Abcam; ab3333; Clone 0.T.21; mouse monoclonal, used at  
578 1:600), Cortactin (Abcam; ab81208; Clone EP1922Y; rabbit monoclonal), Cortactin  
579 (Santa Cruz Biotechnology; sc-30771; G-18; goat polyclonal), MYC (Cell Signaling  
580 Technology, Danvers, MA, USA; mab2278; Clone 71D10; rabbit monoclonal), FLAG  
581 (Sigma; F1804; Clone M2; mouse monoclonal), and EGFP (Roche; 11814460001;  
582 Clones 7.1 and 13.1; mixture mouse monoclonal). Unless otherwise stated, all primary  
583 antibodies were used at 1:200 dilution for immunofluorescence and 1:1,000 for western  
584 blotting.

585 ***In vitro* invasion assay**

586 *In vitro* invasion assays were performed as previously described <sup>39</sup>. In brief,  $1.5 \times 10^5$   
587 cells were plated in the top wells of Growth Factor Reduced Matrigel-coated invasion  
588 chambers (8  $\mu$ m pore size, BD Bio Coat). Media containing 5% was added to the lower  
589 chamber, and cells were allowed to invade along the serum gradient for 18 h at 37°C.  
590 The assay was fixed with 3.7% PFA for 20 min and stained with NucBlue (Invitrogen) to  
591 visualize the nuclei. When siRNA-transfected cells were used, siGLO-Red (Dharmacon,  
592 Lafayette, CO, USA) was co-transfected in the cells to identify siRNA-treated cells. The  
593 membrane was detached from the chamber and mounted on a coverslip, and 10  
594 random fields of view were imaged across the membrane at 20 $\times$  magnification on an  
595 IX81-ZDC microscope (Olympus, Tokyo, Japan). The number of invading cells was  
596 counted manually with ImageJ software by thresholding onto the nucleus, and data are  
597 reported as the means of 3 experiments for each condition.

598 **Invadopodia lifetime assay**

599 MTLn3 cells were transfected with cortactin-miRFP703 and EGFP-Tks5<sup>68</sup> before plating  
600 on gelatin-coated coverslips for 16 h. The cells were imaged every 2 min for 4 h on an  
601 IX81-ZDC inverted epifluorescence microscope at 60× magnification (Olympus).  
602 Invadopodia lifetimes were quantified manually for at least 30 invadopodia from at least  
603 10 cells per condition in at least 3 experiments. Control and siRNA conditions were  
604 imaged on the same day for each experiment. Cells expressing siRNA and scrRNA  
605 were identified by co-transfection with siGLO-Red (Dharmacon).

606 **Immunoprecipitation and pull-down experiments**

607 HEK293T cells were plated overnight at a density of  $1 \times 10^6$  cells on poly-L-lysine-  
608 coated six-well plates. The FLAG-tagged TC10 mutants and the MYC-tagged WT  
609 Exo70 expression constructs were mixed at a 1:1 ratio, and the cells were transfected  
610 using the polyethyleneimine (PEI) reagent at the optimized 2 µg DNA to 8 µL PEI ratio  
611 for each well, according to published protocols<sup>69</sup>. After 48 h, cells were lysed in a buffer  
612 containing 1% NP-40, 20 mM Tris HCl, pH 7.4, 137 mM NaCl, 10 mM MgCl<sub>2</sub>, 1 mM  
613 PMSF, and 1× protease inhibitor cocktail (Sigma-Aldrich). Lysates were clarified by  
614 centrifugation at 22,000 rcf for 10 min at 4°C. After removing an “input fraction, lysates  
615 were mixed with protein A/G agarose beads (Pierce, Waltham, MA, USA) conjugated to  
616 antibodies against FLAG-tag (Sigma-Aldrich) or Exo70 (Santa Cruz, Dallas, TX, USA),  
617 at a concentration of 2 µg antibody per sample, and incubated overnight at 4°C with  
618 gentle rocking. Samples were washed 3× in lysis buffer, mixed with 5× gel loading  
619 buffer, and boiled for 5 min at 99°C prior to loading separation by SDS-PAGE for  
620 western blotting analysis.

621 Biosensor pull-downs were performed using purified PAK1-PBD-agarose beads, as  
622 previously described<sup>41</sup>. To prepare the glutathione (GSH)-agarose beads, 72 mg of  
623 GSH-agarose (Sigma-Aldrich) was resuspended in 10 ml sterile water and incubated at  
624 4°C for 1 h. The suspension was briefly centrifuged, and the pellet was washed three  
625 times with sterile water, followed by washing two times in a resuspension buffer (50 mM  
626 Tris, pH 8.0, 40 mM EDTA, and 25% sucrose). The washed GSH-agarose slurry was  
627 resuspended in 1 ml of resuspension buffer. To generate GST-PAK1-PBD, pGEX-PBD

628 (a gift from G. Bokoch<sup>70</sup>) was transformed into BL21(DE3)-competent bacteria (Agilent  
629 Technologies, Santa Clara, CA, USA) and grown in a shaker flask at 225 rpm and 37°C  
630 until an optical density of 1.0 at 600 nm was achieved. Protein synthesis was induced  
631 by the addition of 0.2 mM Isopropyl  $\beta$ -d-1-thiogalactopyranoside (IPTG), and the flask  
632 was immediately chilled to RT and incubated at 225 rpm and 24°C overnight. The next  
633 day, bacteria were pelleted and resuspended in 20 ml resuspension buffer containing 1  
634 mM PMSF, 1 $\times$  protease inhibitor cocktail (Sigma-Aldrich), and 2 mM  $\beta$ –  
635 mercaptoethanol and rotated on a Nutator for 20 min at 4°C. After incubation, 8 ml  
636 detergent buffer (50 mM Tris, pH 8.0, 100 mM MgCl<sub>2</sub>, and 0.2% [wt/vol] Triton X-100)  
637 was added, and the mixture was incubated at 4°C for 10 min on a Nutator. After  
638 incubation, the mixture was ultrasonicated (4 $\times$  cycles of 30-s ultrasonication followed by  
639 1 min rest on ice) and centrifuged at 22,000 rcf for 45 min at 4°C. The supernatant was  
640 transferred to a 50-ml tube, and 1 ml previously prepared GSH-agarose beads were  
641 added and incubated at 4°C for 1 h on a Nutator. The beads were then pelleted by a  
642 brief centrifugation step and washed four times with wash buffer (50 mM Tris, pH 7.6,  
643 50 mM NaCl, and 5 mM MgCl<sub>2</sub>) followed by resuspension in 500  $\mu$ l of 50:50  
644 glycerol/wash buffer. Aliquots of this mixture at 50  $\mu$ l aliquots were stored at -80°C until  
645 use. For pull-down experiments, HEK293T cells were transfected and lysed as  
646 described above. Lysates were clarified by centrifugation at 22,000 rcf for 10 min at  
647 4°C. After removing an “input” fraction, lysates were incubated with PAK1-PBD–  
648 conjugated agarose beads for 1 h at 4°C, washed 3 $\times$  in lysis buffer, resuspended in  
649 final sample buffer, and analyzed by western blotting. Incubation with Ponceau S  
650 solution (Sigma-Aldrich) was used to visualize GST-PAK1-PBD to control for equal  
651 loading. Anti-GFP (mouse; 11814460001; clones 7.1 and 13.1 mix; Roche, Basel,  
652 Switzerland) antibody was used to detect the TC10 biosensor or fluorescently tagged  
653 TC10 protein.

#### 654 **Generation of a TC10-knockout cell line using CRISPR-Cas9**

655 Four different 20-nt guide sequences for TC10 were selected using the online CRISPR  
656 Design Tool (<http://tools.genome-engineering.org>) against rat TC10 GTPase.  
657 Sequences for the primer pairs are as follows: sgRNA 1: 5'-

658 CACCGCGTAGTGGTCGAAGACAGT-3' and 5'-AACACTGTCTCGACCACTACGC-  
659 3'; sgRNA 2: 5'-CACCGTGCCTAGTGGTCGAAGACAG-3' and 5'-  
660 AACCTGTCTCGACCACTACGCAC-3'; sgRNA 3: 5'-  
661 CACCGAGGTACTGCTTGCCCCCA-3' and 5'-AAACTGGGGGCAAGCAGTACCTC-  
662 3'; and sgRNA 4: 5'-CACCGGGGGCAAGCAGTACCTCT-3' and 5'-  
663 AACAGAGGTACTGCTTGCCCCC-3'. A negative control NT1 with the sequence 5'-  
664 GCGAGGTATTGGCTCCGCG-3' was also used, which was based on a negative  
665 control sequence from the GeCKOv2 Mouse Library Pool A<sup>71</sup>. sgRNAs were cloned into  
666 the pLentiCRISPR v2 plasmid<sup>71,72</sup> by digestion with *Bsm*BI (New England Biololabs,  
667 Ipswich, MA, USA). pLentiCRISPR v2 was a gift from F. Zhang (Massachusetts Institute  
668 of Technology, Cambridge, MA, USA; 52961; Addgene #52961, Watertown, MA, USA).  
669 The GP2-293 cell line (Takara Bio Inc., Shiga, Japan) was used to produce the  
670 lentivirus by co-transfection with pVSVG, gag-pol, rev, and tat vectors (Takara Bio Inc.).  
671 MTLn3 cells were infected with the lentivirus containing the four TC10-targeting sgRNAs  
672 or the NT1 control sgRNA and were cultured as described in the Cell Culture section.  
673 Transduced cells were selected for the stable incorporation of the CRISPR/Cas9 vector  
674 by puromycin treatment (2 µg/ml). CRISPR knockout efficiency was assessed by  
675 western blotting against TC10 (Fig. 6B). An efficient knockout population was achieved  
676 with sgRNA4, which was used for subsequent experiments.

## 677 Expression cDNA constructs

678 Cortactin–mtagRFP-T<sup>64</sup> and EGFP-Tks5<sup>68</sup> have been previously described. To generate  
679 cortactin-miRFP703, mtagRFP-T was replaced with miRFP703<sup>73</sup>. MT1-MMP-GFP, as  
680 previously described<sup>74</sup>.

681 Full-length human p120RasGAP1 was a gift from D. Esposito (Addgene #70511). To  
682 construct the competitive inhibitor of p190:p120 interaction, the sequence for amino  
683 acids 180 to 474 of the human p120RasGAP1 was PCR amplified, based on the  
684 sequence homology to Rat p120RasGAP1, as published previously<sup>54</sup>. The following  
685 primer pair was used: 5'-  
686 GGAATGTTAAGCAATGGATCCTGGTATCACGGAAAACTTGACAGAAC-3' and 5'-

687 CGAGTACAAGTAATTCATCTCGAGCTAAATGTTTTATAAAAGGCATCCTTG-3'.  
688 The PCR amplified fragment was digested with *Bam*HI and *Xba*l and ligated into the  
689 pTriEX-4 backbone at *Bam*HI/*Xba*l sites. A codon-optimized mScarlet<sup>75</sup> fluorescent  
690 protein was synthesized (Genewiz, South Plainfield, NJ, USA) with an upstream *Nco*I  
691 site and a downstream 10 amino acid linker: GSGSGSGSGG (5'-  
692 GGCAGCGGCTCCGGAGCGGGTCCGGAGGC-3'), followed by a *Bam*HI site, and  
693 inserted into the pTriEX-4 vector containing the 2-3-2 fragment at the *Nco*I/*Bam*HI sites.  
694 To produce the pTriEX-mtagBFP2 version of the p190:p120 competitive inhibitor  
695 construct, the mScarlet fluorescent protein was restriction digested with *Nco*I/*Bam*HI,  
696 and mtagBFP2<sup>76</sup> was 2-step PCR-amplified using the following primer pairs: 5'-  
697 GCAATATAATGAATACCATGGTGTCTAAGGGCGAAGAGCTGAT-3' and 5'-  
698 ACCCGCTCCGGAGCCGCTGCCATTAAAGCTTGTGCCAGTTGCTA-3', followed  
699 by 5'-GCAATATAATGAATACCATGGTGTCTAAGGGCGAAGAGCTGAT-3' and 5'-  
700 GGTAAATAAGTATATCGGATCCGCCCTCCGGACCCGCTCCGGAGCCGCTGCCATT-  
701 3', to encode the 10 amino acid linker GSGSGSGSGG (5'-  
702 GGCAGCGGCTCCGGAGCGGGTCCGGAGGC-3') followed by a *Bam*HI site. The 2-  
703 step PCR-amplified fragment was digested with *Nco*I and *Bam*HI and ligated into the  
704 pTriEX backbone containing the competitive inhibitor fragment.

705 Full-length p190RhoGAP-A (mouse) was previously published<sup>39</sup>. P190RhoGAP-A  
706 mutants were produced through PCR-based site-directed mutagenesis using the  
707 Quikchange kit (Stratagene, San Diego, CA). For the Y1087F mutation, the primer pair:  
708 5'-GGATGGATTGATCCTTCTGACTTCGCAGAGCCCAT-3' and 5'-  
709 ATGGGCTCTGCGAAGTCAGAAGGATCAAATCCATCC-3' was used. For the Y1105F  
710 mutation, the primer pair: 5'-  
711 CAAGGAATGAGGAAGAAAACATATTCTCAGTCCCCAC-3' and 5'-  
712 GTGGGGCACTGAGAATATGTTTCTTCCTCATTCTTG-3' was used. For the  
713 R1283A (catalytically-dead/dominant-negative) mutation, the primer pair: 5'-  
714 GCACTGAAGGCATCTACGCGGTAGTGGAAACAAGT-3' and 5'-  
715 ACTTGTTCCACTGACCGCGTAGATGCCTTCAGTGC-3' was used. To produce a  
716 fluorescent protein-tagged p190RhoGAP-A, the following PCR primers were used:  
717 5'-GCATATATTAAGCAATCAAGAATTGCAAGAAAGCAAGATGTCCGAA-

718 3' and 5'-  
719 GGTTAAATATAGCATATACTCGAGCTACAGCGTGTTCGGCTGGAGC-3'. The  
720 PCR fragment was digested with *Eco*RI and *Xba*I and ligated into the pTriEX backbone  
721 at corresponding *Eco*RI/*Xba*I sites, which contained the appropriate fluorescent protein  
722 at the N-terminal end of the multiple cloning site.

723 Full-length human WT TC10 GTPase cDNA was purchased from [www.cDNA.org](http://www.cDNA.org). TC10  
724 mutants were produced through PCR-based site-directed mutagenesis using the  
725 Quikchange kit (Stratagene). For the Q75L mutation, the primer pair: 5'-  
726 GGTCAAGTCTTCCAGTCCGGCCGTGTCA-3' and 5'-  
727 TGACACGGCCGGACTGGAAGACTATGACC-3' was used. For the T31N mutation, the  
728 primer pair: 5'-CATGAGTAGGCAATTCTTGCACCCACCGCCCCGTC-3' and 5'-  
729 GACGGGGCGGTGGCAAGAATTGCCTACTCATG-3' was used. For the T49A  
730 mutation, the primer pair: 5'-TGGTCGAAGACGGCGGGCACGTACTCC-3' and 5'-  
731 GGAGTACGTGCCGCCGTCTCGACCA-3' was used. For the Y54C mutation, the  
732 primer pair: 5'-ACGCTGACTGCGCAGTGGTCGAAGACGG-3' and 5'-  
733 CCGTCTTCGACCCTGCGCAGTCAGCGT-3' was used. For the G26V mutation, the  
734 primer pair: 5'-TGCCCACCGCCACGTGCGCCGACC-3' and 5'-  
735 GGTCGGCGACGTGGCGGTGGCA-3' was used. For the F42L mutation, the primer  
736 pair: 5'-GCTATGCCAACGACGCCTTACCGGAGGAGT-3' and 5'-  
737 ACTCCTCCGGTAAGGCGTCGTTGGCATAGC-3' was used. For the P43L/E45V/Y46H  
738 mutations, the primer pair: 5'-ACGACGCCCTCCTGGAGGTGCACGTGCCACCG-3'  
739 and 5'-CGGTGGGCACGTGCACCTCCAGGAAGGCGTCG-3' was used. For the  
740 P43L/E45V/Y46H/T49A/Y54C mutations, the primer pair: 5'-  
741 CGACGCCCTCCTGGAGGTGCACGTGCCCGCC-3' and 5'-  
742 GGCGGGCACGTGCACCTCCAGGAAGGCGTCG-3' was used. To generate fusion  
743 constructs containing TC10 and fluorescent proteins or a FLAG-tag, the following primer  
744 pair was used to PCR amplify the TC10 fragment: 5'-  
745 GAGATTATTAGATGATATAGAATTGATGCCGGAGCCGGCCGCAGCAGCAT-3' and  
746 5'-GCTATGCATATAATATAATCCTCGAGTCACGTAATTAAACAAACAGTTATACATC-  
747 3'. The PCR-amplified fragment was digested with *Eco*RI/*Xba*I and ligated into the  
748 pTriEX backbone, which contained the appropriate fusion tags at *Eco*RI/*Xba*I sites.

749 **siRNA**

750 siRNA Smart pools for TC10, p190RhoGAP, p120RasGAP were purchased from  
751 Dhamacon/GE Healthcare (siGenome). Transfections were performed with  
752 Oligofectamine 2000 (Invitrogen) for MTLn3 cells and via electroporation, using Amixa  
753 cell line nucleofector kit V (VACA 1003, Lonza, Basel, Switzerland), for MDA-MB-231  
754 cells. To monitor the transfection efficiency, siGLO-Red (Dharmacon) was co-  
755 transfected, according to the manufacturer's protocols. Knockdown was assessed, and  
756 subsequent assays were performed at 48 h (MTLn3) or 72 h (MDA-MB-231) after  
757 transfection.

758 **TC10 biosensor**

759 A FRET biosensor for TC10 was constructed based on the previously published Rac-  
760 type, single-chain, genetically encoded biosensor backbone system<sup>41</sup>. Briefly, WT and  
761 mutant human TC10 GTPase sequences were PCR-amplified using the primer pair: 5'-  
762 GAGATTATTAGATGATAGAATTGATGCCGGAGCCGGCCGCAGCAGCAT-3' and  
763 5'-GCTATGCATATAATATAATCCTCGAGTCACGTAATTAAACAACAGTTATACATC-  
764 3' and restriction digested with *Eco*RI and *Xba*l. The digested fragments were ligated  
765 into the pTriEX-4 vector containing the Rac1 FRET biosensor backbone<sup>41</sup> at the  
766 *Eco*RI/*Xba*l sites to exchange the Rac1 GTPase sequence for the TC10 GTPase  
767 fragments. This sensor backbone was previously codon-optimized with synonymous  
768 modifications<sup>77</sup> to improve the stability and expression fidelity of the biosensor in target  
769 cells. To generate the retroviral vector containing the biosensor in the tet-inducible  
770 system, the pRetro-X vector system (Clontech, Mountainview, CA, USA) was used.  
771 Briefly, pRetro-X-puro (Clontech) was modified by inserting a Gateway destination (-  
772 DEST) cloning cassette (Invitrogen) into the multiple cloning site. The pTriEX-TC10  
773 biosensor was restriction digested using *Ncol* and *Xba*l to extract the TC10 biosensor  
774 as a full-length cassette, which was then ligated into the pENTR-4 vector (Invitrogen) at  
775 *Ncol*/*Xba*l sites. The pENTR-TC10 biosensor was then processed for Gateway cloning,  
776 together with the pRetro-X-Puro-DEST vector, using LR Clonase II (Invitrogen),  
777 following the manufacturer's protocols. The resulting pRetro-X-Puro-TC10 biosensor

778 was used to produce the retrovirus used to infect cells to produce stable/inducible tet-  
779 OFF biosensor cell lines, as previously described<sup>44</sup>.

780 **Microscopy imaging**

781 MTLn3 or MDA-MB-231 cells were plated at a cell density of  $1.5 \times 10^5$  on gelatin-coated  
782 glass coverslips. For fixed-cell imaging, cells were fixed for 15 min with 1% PFA in PBS  
783 and processed for immunofluorescence 16 hours after plating. A widefield imaging  
784 modality was used to obtain immunofluorescence images. For colocalization analyses,  
785 z-stacks were imaged using 0.2- $\mu\text{m}$  z-steps for 26 steps, centered on the in-focus  
786 plane, and the resultant z-stacks were deconvolved (Microvolution, Cupertino, CA,  
787 USA) to remove out of focus light. For live-cell imaging, the imaging medium was  
788 prepared by using Ham's F12K medium, without phenol red (Crystalgen, Commack,  
789 NY, USA), and supplemented with 1 $\times$  glutamine, and sparged with Argon gas for 1 min  
790 to reduce the dissolved oxygen concentration. The medium was supplemented with 5%  
791 FBS, Oxyfluor Reagent (1:100 dilution, Oxyrase Inc., Mansfield, OH, USA), and 10 mM  
792 dl-lactate (Sigma-Aldrich)<sup>78</sup>. Cells were imaged at 37°C in a closed chamber<sup>44</sup> mounted  
793 on an inverted microscope stage. Images were acquired through a 60 $\times$  magnification  
794 objective lens (UIS 60 $\times$  1.45 NA; Olympus) using a custom microscope<sup>79</sup> capable of the  
795 simultaneous acquisition of FRET and mCerulean emissions through two Coolsnap ES2  
796 cameras (Photometrics, Tucson, AZ, USA) that are mounted via an optical beam splitter  
797 and containing a T505LPXR mirror, ET480/40M for mCerulean emission, and  
798 ET535/30M for mVenus-FRET emission (Chroma Technology Corp, Bellows Falls, VT,  
799 USA). The relative intensities between the two channels were balanced by the inclusion  
800 of a neutral density filter (ND0.2 in mCerulean channel) to ensure that the range of  
801 brightness in both mCerulean and FRET channels were similar to maximize the signal  
802 to noise ratio. Cells were illuminated with a 100W Hg arc lamp through a neutral density  
803 filter to attenuate light as needed and then through an ET436/20X bandpass filter for  
804 mCerulean excitation. The main fluorescence turret of the microscope contained a  
805 20/80 mirror (Chroma Technology) that allowed 20% of the excitation illumination to  
806 reach the specimen and 80% of the emitted light to pass through to detection. The  
807 IX81ZDC microscope was fitted with a T555LPXR longpass mirror within the internal

808 port-switching prism holder to direct the biosensor emission channels to the left-hand  
809 side port of the microscope and direct the longer wavelengths, including the cortactin  
810 and differential interference contrast (DIC) channels, to the bottom port of the  
811 microscope. The bottom port of the microscope was fitted with a single Coolsnap HQ2  
812 camera (Photometrics) via either FF585/29 emission filter for mtagRFP-T to detect  
813 cortactin fluorescence or an aligned linear polarizer to detect the DIC illumination.  
814 MetaMorph software (Molecular Devices) was used to control the microscope, motion  
815 control devices, and image acquisition. MetaMorph and MatLab software (ver 2011a;  
816 Mathworks, Natick, MA, USA) were used to perform image processing and data  
817 analyses, as previously described<sup>38,41,44</sup>. Image processing included camera noise  
818 subtraction, flatfield correction, background subtraction, image registration, ratio  
819 calculations, and correction for photobleaching<sup>80</sup>. In brief, camera noise images were  
820 acquired at the same exposure times as the foreground image sets but without the field  
821 illumination. This represented the camera read noise and the dark current noise and  
822 was subtracted from all subsequent foreground images. Flatfield correction involved the  
823 acquisition of cell-free fields of view with the same exposure and field illumination  
824 conditions as the foreground image sets, followed by camera noise subtracted to obtain  
825 the shading images. The camera noise–subtracted foreground images were then  
826 divided by the shading images to obtain flatfield-corrected images. A small region of  
827 interest in the background (cell-free) area was selected in the flatfield-corrected  
828 foreground image sets, and the mean gray value from such a region was subtracted  
829 from the whole field of view, calculated, and processed at each time point to obtain the  
830 background-subtracted image sets. The background-subtracted image sets were then  
831 subjected to an affine transformation based, on a priori calibration, to account for  
832 misalignments between the three cameras used for the simultaneous imaging of the  
833 FRET and mCerulean channels, plus the cortactin and DIC channels in the longer  
834 wavelengths. After the transformation, a linear X–Y registration was performed on the  
835 resulting image sets, before ratio calculations, in which the FRET image set was divided  
836 by the mCerulean channel image set. For photobleaching corrections of the ratio image  
837 set, whole-cell mean gray values were calculated at each time point and fitted to a  
838 biexponential decay model. The inverse function of the regressed model was then

839 multiplied into the ratio image set to approximate the effect of photobleaching. For fixed-  
840 cell biosensor imaging, a single Coolsnap HQ2 camera (Photometrics) attached to the  
841 bottom port of the microscope was used, together with a 60 $\times$  magnification objective  
842 lens. In this case, excitation and emission filter wheels switched appropriate filter sets,  
843 in addition to the appropriate neutral density filters, to acquire mCerulean and FRET  
844 emissions plus any other additional wavelengths, as required. For the imaging of  
845 biosensors, we adjusted the camera acquisition time duration by targeting to fill  
846 approximately 80% of the total digitization range of the charge-coupled device circuitry,  
847 to maximize the dynamic range, using excitation light intensities of 0.4–1.0 mW at the  
848 specimen plane.

#### 849 **Fluorometric characterization and validation of the biosensor**

850 The characterization of the biosensor response was performed in HEK293T cells by  
851 transiently overexpressing WT or mutant versions of the biosensor with or without the  
852 appropriate upstream regulators, as described previously<sup>81,82</sup>. In brief, HEK293T cells  
853 were plated overnight at 1  $\times$  10<sup>6</sup> cells/well in six-well plates coated with poly-L-lysine  
854 (Sigma-Aldrich) and transfected the following day using PEI reagent according to the  
855 published optimized procedures<sup>69</sup>. After 48 h transfection, cells were washed once with  
856 PBS, briefly trypsinized, and resuspended in 500  $\mu$ L of cold PBS per well. Cell  
857 suspensions were stored on ice until assay. Fluorescence emission spectra were  
858 measured with a spectrofluorometer (Horiba-Jobin-Yvon Fluorolog-3MF2; HORIBA,  
859 Kyoto, Japan). The fluorescence emission spectra were obtained by exciting the cell  
860 suspension in a 500  $\mu$ L quartz cuvette (Starna Cells, Atascadero, CA, USA) at 433 nm,  
861 and emission fluorescence was scanned between 450–600 nm. The background  
862 fluorescence reading of cells containing an empty vector (pCDNA3.1) was used to  
863 measure light scatter and autofluorescence and was subtracted from the data. The  
864 resulting spectra were normalized to the peak of the donor mCerulean emission  
865 intensity at 474 nm to generate the final ratiometric spectra. To validate the biosensor in  
866 cancer cells using exogenous stimulation, MTLn3 cells transiently expressing the  
867 biosensor were serum-starved for 4 h and stimulated using medium containing 5%

868 serum or 5 nM EGF. Cells were fixed and imaged at 0, 1, 2, and 3 min after stimulation  
869 and analyzed for changes in the FRET/donor ratio.

870 **Biosensor activity analysis at invadopodia**

871 A time-lapse series of the region of interest containing an invadopodium was analyzed  
872 first by producing time projections. The cortactin core location image was calculated by  
873 obtaining the median projection, over time, of the cortactin channel. TC10 activity  
874 localizations were calculated by taking the summation of intensities over time at the  
875 invadopodium region of interest in a time-lapse stack, as previously described for a  
876 different class of Rho GTPase activity measurements at invadopodia<sup>39</sup>. Line scans were  
877 measured and averaged over 4 perpendicular lines that were centered on the core of  
878 the cortactin spot, with each line rotationally 45 degrees apart. Line scans were  
879 normalized to the local maxima of TC10 activity at the ring-like region surrounding the  
880 invadopodia core, which was denoted by the cortactin spot. The cortactin intensity was  
881 normalized at the center position, taken as the maximal intensity location along the line  
882 scans.

883 For experiments measuring the frequency ratio of high biosensor activity at invadopodia  
884 during transient invadopodia formation, we identified regions of cells featuring the  
885 formation of nascent invadopodium in a time-lapse experiment under steady-state  
886 conditions. The cortactin image stack was used to identify and select an elliptical region  
887 of interest in which the invadopodium core was transiently developing. A random region  
888 was also chosen away from all cortactin spots to serve as the background, and both  
889 regions were tracked for average intensity values over the entire time course of an  
890 experiment. The regions of interest were transferred to the respective biosensor ratio  
891 data stack, and the average biosensor intensity values were also measured as a  
892 function of time. The average foreground intensities over time and the standard  
893 deviation (SD) were calculated from the data, as follows: for data corresponding to the  
894 regions with cortactin spot formation, the average and SD were calculated up to the  
895 time point at which a nascent invadopodia formation became visible; for the random  
896 background control region, the average and SD were measured for the entire duration

897 of the time-lapse experiment. The data were then thresholded at +1.0 SD away from the  
898 mean, and any activity values above this threshold were considered to be positive  
899 biosensor activity events. The total number of positive biosensor activity events were  
900 divided by the total number of time points in the corresponding time domains (“before”  
901 or “during” invadopodia formation, as determined from the cortactin data stack), and the  
902 resulting positive activity event per time data “during” invadopodia formation were  
903 normalized against the values from “before” invadopodia formation.

904 **Autocorrelation analysis for periodicity**

905 For the fluctuation analysis, a binary mask was created in MetaMorph using cortactin  
906 fluorescence intensity as a reference to designate the core of the invadopodium.  
907 Subsequently, this mask was dilated 30 pixels, and the original core was subtracted to  
908 generate a binary mask to designate the invadopodia ring-like region surrounding the  
909 core. These binary masks were used to measure the intensity in each compartment of  
910 the invadopodium. The area of the ring was based on a spatial distance of 1.74  $\mu$ m  
911 radius outside of the core, which is similar to the binary mask used in a previous work<sup>39</sup>.  
912 To quantitatively determine the periodicity of biosensor activity fluctuations within the  
913 core of an invadopodium versus the ring surrounding the invadopodium, a time series of  
914 the ratio of intensities was measured within binary masks that were generated to target  
915 either the invadopodium core or the ring surrounding the invadopodium core. These  
916 ratio time series were analyzed using the autocorrelation function `xcov` in MatLab. The  
917 individual autocorrelation function distribution was smooth-spline fitted, pooled between  
918 all invadopodia analyzed in all cells, and the mean autocorrelation function and 95%  
919 confidence intervals were calculated by a nonparametric bootstrap method<sup>83</sup>. The  
920 measured temporal width to the peaks of the first side lobes after the zero-crossing was  
921 taken as the period of oscillation<sup>45</sup>.

922 **Analysis of tumor intravasation and metastasis *in vivo***

923 MTLn3 cells that stably expressed EGFP and featured the CRISPR/Cas9-mediated  
924 TC10 deletion were injected into the mammary glands of female SCID mice (6–8-wk-  
925 old; Jackson ImmunoResearch Laboratories, Inc., West Grove, PA, USA<sup>84</sup>). A total of

926 1.0 × 10<sup>6</sup> cells were trypsinized and resuspended in 100 µl PBS for injection into each  
927 mouse (CRISPR/Cas9 non-targeting control, n = 20 mice; TC10-knockout, n = 20 mice).  
928 Mice were sacrificed 3–4 wk after injection when the primary tumor reached 1 cm in  
929 diameter. Lung metastases were confirmed and counted at necropsy using a  
930 fluorescent microscope to image EGFP fluorescence in freshly excised and isolated  
931 lungs mounted on a microscope coverslip. Twenty randomly selected fields of view at  
932 10× magnification per mouse lung (10 fields of view per lung lobe) were analyzed to  
933 determine the ratio between total EGFP fluorescence and background fluorescence. To  
934 quantify the circulating tumor cell counts, 1 ml of mouse blood, obtained through  
935 cardiopuncture at the time of euthanasia, was lysed in red blood cell lysis buffer (04-  
936 4300-54; Thermo Fisher Scientific/eBioscience, San Diego, CA, USA), according to the  
937 manufacturer's protocols. The remaining cells were plated into MTLn3 growth media  
938 and cultured for one additional week. The numbers of EGFP-positive MTLn3 cells were  
939 quantified in 1/4 of the area of a 10-cm tissue culture dish for each animal. All animal  
940 experiments were performed in accordance with a protocol approved by the Office of  
941 the Institutional Animal Care and Use Committee of the Albert Einstein College of  
942 Medicine (protocol 20170507). For data analysis, mice with primary tumors that showed  
943 indications of ulceration or intraperitoneal growths were omitted from the final tally.

944 **Statistical analysis:**

945 All statistical significance based on p-values were calculated using a Student's *t*-test,  
946 unless stated otherwise in the figure legend. No vertebrate animals were involved. No  
947 statistical methods were used to pre-determine the sample size. No randomizations  
948 were used. The investigators were not blinded to allocation during experiments and  
949 outcome assessment. Statistical tests used are stated on every figure legend with p-  
950 values as appropriate. Data distribution should meet the normal distribution  
951 requirements. No estimate of variation. No pre-established criteria were used to  
952 determine data inclusion or exclusion.

953 **Data availability.**

954 The data that support the findings of this study are available from the corresponding  
955 author on request.

956 **Code availability.**

957 All Matlab codes and Metamorph scripts used were previously published elsewhere  
958 <sup>45,46,80</sup>, but are also available from the corresponding author on request.

959

960

## 961 **Figure legends**

### 962 **Figure 1: TC10 is localized at invadopodia and is required for matrix degradation.**

963 **a.** Representative localization of endogenous TC10 in rat mammary adenocarcinoma  
964 MTLn3 cells. Cortactin is shown to denote invadopodia structures. White box area is  
965 enlarged to show colocalizations (bottom), showing cortactin, Tks5 and TC10  
966 localizations. White bar = 10- $\mu$ m (top); 2- $\mu$ m (bottom). **b.** Representative, enlarged view  
967 of the immunostaining of cortactin and Tks5 with TC10-WT-mCherry expression. White  
968 bar = 1- $\mu$ m. The “side” localizations (yellow circle) were identified within a dilated  
969 circular region of approximately 30 pixels from the invadopodia core (dashed white  
970 circle). Black arrows point to TC10 localizations. **c.** Quantification of TC10-WT-mScarlet  
971 localization at invadopodia structures. Student’s t-test, two-tail analysis: \*\* p=0.001112;  
972 n=5 experiments; shown with SEM **d.** Quantification of TC10-WT-mCherry localization  
973 in MTLn3 cells stimulated with 5 nM EGF for the indicated times. Results were  
974 normalized to t = 0-min values for both side and core localized fractions. Student’s t-  
975 test, two-tail analysis: ns p=0.5602 for 1-min side versus core; p=0.5688 for 3-min side  
976 versus core; \* p=0.01090 for 5-min side versus core; n=4 experiments; shown with  
977 SEM. **e.** Representative images from siRNA-mediated TC10 depletion in MDA-MB-231  
978 cells impacting gelatin matrix degradation, visualized using a 405-nm fluorescent gelatin  
979 matrix. Invadopodia are denoted by cortactin and Tks5 colocalization with spots of  
980 matrix degradation (arrow). White bar = 10- $\mu$ m. **f.** Quantification of the MDA-MB-231  
981 matrix degradation when TC10 is depleted, shown in (e), normalized to the Ctrl.  
982 Student’s t-test, one-tail analysis: \* p=0.01528; n=3 experiments; shown with SEM. **g.**  
983 siRNA-mediated TC10 depletion in MTLn3 cells and rescue mediated by the  
984 overexpression of wild-type TC10. Results are normalized against Ctrl. Student’s t-test,  
985 one-tail analysis: \*\* p=0.004146; two-tail analysis: ns p=0.9669; n=3 experiments;  
986 shown with SEM. **h.** Total number of steady-state invadopodia/cell in TC10-depleted  
987 MTLn3 cells normalized to Ctrl MTLn3 cells. Student’s t-test, two-tail analysis: \*\*  
988 p=0.7994; n=3 experiments; shown with SEM. **i.** Invadopodia lifetimes in MTLn3 cells,  
989 shown as a histogram with bins corresponding to 20-min intervals. Student’s t-test, two-  
990 tail analysis: ns, p=0.1106 for 0-19 min; p=0.4472 for 20-40 min; p=0.6922 for 41-60

991 min; p=0.09957 for >60 min; n=3 experiments, shown with SEM. **j.** Overexpression of  
992 the GTP hydrolysis-deficient TC10 Q75L mutant in MTLn3 cells plated on a 405-nm  
993 fluorescent gelatin matrix, normalized to Ctrl overexpressing wild-type TC10. Student's  
994 t-test, one-tail analysis: \* P=0.01349; n=3 experiments; shown with SEM. paired one-tail  
995 **k.** Total number of steady-state invadopodia in cells overexpressing wild-type TC10 or  
996 the Q75L mutant, normalized to the Ctrl overexpressing the wild-type TC10. Student's t-  
997 test, two-tail analysis: ns P=0.4824; n=3 experiments; shown with SEM. siRNA  
998 depletion characterizations are shown in Supplementary Figures S2 and S3.

999 **Figure 2: TC10 regulates MT1-MMP cell surface exposure at the plasma**  
1000 **membrane of invadopodia.**

1001 **a.** Representative, localization of endogenous MT1-MMP at invadopodia in MTLn3 cells.  
1002 Invadopodia are denoted by cortactin staining. White bar in top left = 5- $\mu$ m; top right =  
1003 10- $\mu$ m; zoomed views = 1- $\mu$ m. **b.** Quantification of MT1-MMP-WT-GFP localization in  
1004 MDA-MB-231, either within the invadopodia core or on the lateral sides of the core.  
1005 Invadopodia cores are denoted by the colocalization of cortactin and Tks5 signals.  
1006 Student's t-test, two-tail analysis: \*\* p=0.003055; n=3 experiments; shown with SEM.  
1007 Data from MTLn3 cells shown similar trend is shown in Supplementary Figure S4a. **c.**  
1008 The extracellular surface presentation of MT1-MMP at invadopodia requires TC10 in  
1009 MTLn3 cells. The ratio between numbers of invadopodia with cytoplasmic (total) MT1-  
1010 MMP and those featuring surface (ext.) MT1-MMP in cells treated with Ctrl (gray) or  
1011 TC10 siRNA (blue). The ratio of total MT1-MMP-positive invadopodia counts in cells  
1012 treated with Ctrl and TC10 siRNA (magenta), indicating that only the surface  
1013 presentation of MT1-MMP is impacted by TC10 depletion. TC10-KD data are  
1014 normalized to the Ctrl-ext. over total ratio. Student's t-test, one-tail analysis: \*\*  
1015 p=0.005750; n=3 experiments; shown with SEM. **d.** Representative, immunostaining of  
1016 TC10 and Exo70 at the invadopodia site in MTLn3 cells, showing the side and the core  
1017 localizations. White bar in top = 10- $\mu$ m; zoomed views = 1- $\mu$ m. **e.** The quantification of  
1018 TC10 and exo70 localization at invadopodia in MTLn3 cells, as shown in (d), normalized  
1019 to the core % for TC10 and Exo70, respectively. Student's t-test, two-tail analysis: \*\*  
1020 p=0.007508; \* p=0.01124; n=8 experiments; shown with SEM. **f.** Immunoprecipitation of

1021 wild-type (WT) Exo70 and TC10 mutants, overexpressed in HEK293T cells. Lanes: 1,  
1022 untransfected; 2, WT TC10; 3, F42L TC10; 4, Q75L TC10; 5, T31N TC10; 6,  
1023 P43L/E45V/Y46H (3 $\times$  mut) TC10; and 7, P43L/E45V/Y46H/T49A/Y54C (5 $\times$  mut) TC10.  
1024 Full-sized western blots are shown in Supplementary Figure S13. **g.** Matrix degradation  
1025 per cell, comparing WT TC10 and 5 $\times$  mut TC10, overexpressed in MTLn3 cells, as  
1026 plated on a 405-nm fluorescent gelatin matrix. Results are normalized to the Ctrl.  
1027 Student's t-test, paired one-tail analysis: \*\* p=0.005604; n=5 experiments; shown with  
1028 SEM. **h.** Total number of steady-state invadopodia, comparing WT TC10 and 5 $\times$  mut  
1029 TC10, overexpressed in MTLn3 cells. Results are normalized to the Ctrl. Student's t-  
1030 test, paired two-tail analysis: ns p=0.7283; n=5 experiments; shown with SEM. **i.**  
1031 Localization of exo70 at invadopodia (core/side/no localization) in MTLn3 cells,  
1032 comparing the overexpression of WT TC10 and 5 $\times$  mut TC10. Student's t-test, paired  
1033 two-tail analysis: \*\* p=0.002105; \* p=0.01138; ## p=0.00003960 n=5 experiments;  
1034 shown with SEM.

1035 **Figure 3: TC10 activity at invadopodia is spatially regulated.**

1036 **a.** A schematic cartoon of the single-chain, genetically encoded FRET biosensor for  
1037 TC10 GTPase, based on previous biosensor designs used to evaluate Rac/Cdc42-type  
1038 GTPases<sup>38,40-42</sup>. The FRET donor (cyan) and acceptor (yellow) were mCerulean1 and  
1039 circularly permuted mVenus, respectively. We also produced a near-infrared version  
1040 of the TC10 FRET biosensor, which behaved similarly to the cyan-yellow version based  
1041 on a previous design (Supplementary Fig. S6)<sup>85</sup>. **b.** Representative, normalized  
1042 fluorescence emission spectra of the constitutively activated (CA: Q75L) versus the  
1043 dominant-negative (DN: T31N) versions of the TC10 biosensor upon excitation at 433  
1044 nm when overexpressed in HEK293T cells and measured in cell suspensions. Spectra  
1045 were normalized to the peaks of the donor emission at 474 nm. **c.** Fluorometric  
1046 emission ratio of the TC10 biosensor overexpressed in HEK293T cells. WT biosensor  
1047 expression and the Q75L and G26V CA mutant biosensors showed high emission  
1048 ratios. The DN biosensor, CA biosensors with GTPase binding-deficient mutations in  
1049 both PBD domains (Q75L-H83/86D), and effector binding mutants (T49A, Y54C)  
1050 showed low emission ratios. Student's t-test, two-tail analysis: ns p=0.06587 for Q75L,

1051 p=0.3810 for G26V; \*\* p=1.544x10<sup>-6</sup> for T31N, p=0.001531 for Q75L-H83/86D,  
1052 p=0.0001294 for T49A, and p=0.0001279 for Y54C, all compared to the WT (first bar);  
1053 n=7 experiments for WT, 4 experiments for all other conditions, all shown with SEM. **d.**  
1054 The co-expression between p50RhoGAP, p190RhoGAP, and the non-targeting  
1055 Rap1GAP1 and the WT TC10 biosensor. Student's t-test, two-tail analysis: ##  
1056 p=9.899x10<sup>-5</sup>, \*\* p=0.003775, ns p=0.3204, all compared to the WT TC10 biosensor  
1057 expression (first bar) without GAP co-expression. N=7 experiments for WT, n=3  
1058 experiments for p50RhoGAP and Rap1GAP and n=4 experiments for p190RhoGAP co-  
1059 expressions, shown with SEM. **e.** Representative, dynamic localization patterns of TC10  
1060 activity at and surrounding the invadopodium core (denoted by cortactin fluorescence).  
1061 Time-lapse sequence intervals are 10 seconds. **f.** The line scan analysis of the intensity  
1062 distributions across invadopodia showing normalized TC10 activity integrated over time,  
1063 plotted against the matching cortactin intensity distributions. The blue-shaded regions  
1064 indicate significant (p < 0.05; Student's t-test, one-tail; n = 33 invadopodia from 19 cells  
1065 over 7 experiments; for p-value distributions, see Appendix 1) differences in TC10  
1066 activity intensity compared with the invadopodia core center at 0.0  $\mu$ m. Line scans were  
1067 normalized to the local maxima of TC10 activity at the ring-like region surrounding the  
1068 invadopodia core, which was denoted by the cortactin spot. The cortactin intensity was  
1069 normalized at the center position, taken as the maximal intensity location along the line  
1070 scans. **g.** Autocorrelation functions showing fluctuations in TC10 activity in the  
1071 invadopodia core (red) versus the ring-like region (blue) around the invadopodia core.  
1072 The gray lines (solid: core; dashed: ring) indicate the 95% confidence intervals around  
1073 the mean. N = 29 invadopodia core and ring measurements, from 19 different cells, in 8  
1074 experiments.

1075 **Figure 4: p190RhoGAP impacts invadopodia function by targeting TC10.**

1076 **a.** Representative, immunostaining of endogenous p190RhoGAP at the invadopodia  
1077 core, in MTLn3 cells. White bar = 1- $\mu$ m. **b.** The percentage of invadopodia with  
1078 p190RhoGAP localization in MTLn3 cells, following starvation and EGF stimulation (5  
1079 nM) for the indicated times. The steady state percentage of invadopodia with  
1080 p190RhoGAP localization in MTLn3 cells in serum is also shown. Student's t-test, two-

1081 tail analysis: ns p=0.7220, steady state versus 0 min; p=0.9730, 0 min versus 3 min;  
1082 p=0.8520, 0min versus 5 min; n=3 experiments; shown with SEM. **c.** Matrix degradation  
1083 from MTLn3 cells transfected with control siRNA (Ctrl, gray) or siRNA against  
1084 p190RhoGAP (KD, blue), and the overexpression of a catalytically dead p190RhoGAP  
1085 dominant-negative mutant (DN, pink). Results are normalized to the Ctrl. p190RhoGAP  
1086 depletion characterization and efficiency evaluations are shown in Supplementary  
1087 Figure S8. Student's t-test, two-tail analysis: \*\* p=0.006336; n=3 experiments; shown  
1088 with SEM; \* p= 0.04141; n=4 experiments; shown with SEM. **d.** Invadopodia lifetime  
1089 assay in MTLn3 cells transfected with Ctrl versus p190RhoGAP siRNA. Student's t-test,  
1090 two-tail analysis: ns, p= 0.5646 for 0-19 min; p=0.9495 for 20-39 min; p=0.6673 for 40-  
1091 59 min; p=0.7356 for >60 min; n=3 experiments, shown with SEM. **e.** The localization of  
1092 TC10 in MTLn3 cells transfected with Ctrl or p190RhoGAP siRNA. Student's t-test, one-  
1093 tail analysis: \*\* p=0.005126; n=4 experiments; shown with SEM; Student's t-test, paired  
1094 one-tail analysis: \* p= 0.033138; # p=0.03791; n=4 experiments; shown with SEM. **f.**  
1095 The percentage of invadopodia with extracellular, endogenous MT1-MMP localization  
1096 from among 231 cells, transfected with either Ctrl or p190RhoGAP siRNA. Student's t-  
1097 test, paired one-tail analysis: \* p=0.02492; n=3 experiments; shown with SEM. **g.**  
1098 Representative example images of TC10 biosensor activity at an invadopodium in  
1099 MTLn3 cells transfected with p190RhoGAP siRNA. The invadopodium is denoted by the  
1100 cortactin fluorescence signal. **h.** The line scan analysis of the intensity distributions  
1101 across invadopodia for TC10 activity integrated over time, showing the p190RhoGAP-  
1102 depleted condition, together with the normalized cortactin trace. The blue-shaded  
1103 regions indicate significant (p < 0.05; Student's t-test, one-tailed; n = 25 invadopodia  
1104 from 12 cells over 3 experiments; For p-value distributions, see Appendix 1) differences  
1105 from the TC10 activity intensity at the center of the invadopodia core at 0.0  $\mu$ m. TC10  
1106 activity line scans were normalized to the position at the ring-like region surrounding the  
1107 invadopodia core, as determined and shown in Figure 3g. The cortactin intensity was  
1108 normalized at the center position, taken as the maximal intensity location along the line  
1109 scans. **i.** Autocorrelation functions for the fluctuation of TC10 activity when  
1110 p190RhoGAP is depleted in the invadopodium core (red) versus the ring-like region  
1111 (blue) around the invadopodium core. The gray lines (solid: core; dashed: ring) indicate

1112 the 95% confidence intervals around the mean. The autocorrelation function in the core  
1113 of invadopodia does not appear to inflect after the first zero-crossing (no periodicity).  
1114 The autocorrelation function in the ring-like region has repeating inflection patterns that  
1115 cross zero several times at a measurable periodicity (inflection points are indicated with  
1116 blue arrows) of approximately  $229 \pm 28$  seconds. N = 18 invadopodia core and ring  
1117 measurements from 10 different cells in 3 experiments. **j.** The absolute values of the  
1118 amplitude of fluctuation in the TC10 biosensor activity in the core versus the ring-like  
1119 region around invadopodium core. The data are normalized to the core fluctuation  
1120 amplitudes in the WT condition (first bar). Student's t-test, two-tail analysis: ns p=  
1121 0.2546 (WT core versus WT ring), ns p= 0.4415 (WT core versus p190KD core), \* p=  
1122 0.03771 (p190KD core versus p190KD ring); n = 29 invadopodia core and ring  
1123 measurements for WT, from 19 different cells, in 8 experiments, and n = 18 invadopodia  
1124 core and ring measurements for p190KD from 10 different cells in 3 experiments; shown  
1125 with SEM.

1126 **Figure 5: Tyrosine phosphorylation of p190RhoGAP is required for matrix  
1127 degradation**

1128 **a.** Representative, immunostaining for endogenous p190RhoGAP and Y1105-  
1129 phosphorylated p190RhoGAP, co-expressed with mtagRFP-T-cortactin as an  
1130 invadopodia marker. White bar = 5- $\mu$ m. **b.** Quantification of the percentage of  
1131 invadopodia that were positive for phosphorylated p190RhoGAP colocalization.  
1132 Student's t-test, two-tail analysis: \*\* p=0.0001518; n=3 experiments, shown with SEM.  
1133 **c.** The ratio of phosphorylated p190RhoGAP to total p190RhoGAP at invadopodia in  
1134 MTLn3 cells during invadopodia precursor formation, induced by 5 nM EGF treatment  
1135 following starvation for the indicated times. Results are normalized to the ratio at 0-min.  
1136 Student's t-test, two-tail analysis: "ns" p=0.742460426 for 0 min – 1 min;  
1137 p=0.120533868 for 0 min – 3 min; and \*\* p=0.007470 for 0 min – 5 min; n=3  
1138 experiments, shown with SEM. **d.** Representative, immunostaining of endogenous  
1139 p190RhoGAP and p120RasGAP at invadopodia, shown together with the co-expression  
1140 of fluorescent protein-tagged WT TC10 and cortactin. White bar = 1- $\mu$ m. **e.**  
1141 Quantification of endogenous p190RhoGAP and p120RasGAP localization at either the

1142 core or the side of invadopodia. Student's t-test, two-tail analysis: "ns" p= 0.3618 for  
1143 TC10 core vs. side; \* p=0.01146 for p190 core vs. side; # p=0.04271 for p120 core vs.  
1144 side; n=3 experiments, shown with SEM. **f.** Quantification of the change in  
1145 p190RhoGAP localization upon overexpression of the p190:p120 competitive binding  
1146 inhibitor. Student's t-test, two-tail analysis, \*\* p=0.00006365; ## p=0.002991; "ns"  
1147 p=0.5417; n=3 experiments, shown with SEM. **g.** Quantification of matrix degradation by  
1148 MTLn3 cells when the p190:p120 competitive binding inhibitor was overexpressed.  
1149 Results are normalized to the Ctrl where only the fluorescent protein was  
1150 overexpressed. Student's t-test, two-tail analysis: \*\* p= 0.0005644; n=3 experiments,  
1151 shown with SEM. **h.** The number of steady-state invadopodia in MTLn3 cells when the  
1152 p190:p120 competitive binding inhibitor was overexpressed. Results are normalized to  
1153 the Ctrl where only the fluorescent protein was overexpressed. Student's t-test, two-tail  
1154 analysis: "ns" p=0.5016; n=3 experiments, shown with SEM. **i.** Quantification of the  
1155 matrix degradation by MTLn3 cells when a Y1105/1087 phosphorylation-deficient  
1156 mutant version of p190RhoGAP was overexpressed. Results are normalized to the Ctrl  
1157 where only the fluorescent protein was overexpressed. Student's t-test, two-tail  
1158 analysis: \*\* p= 0.002018; n=3 experiments, shown with SEM. **j.** The number of steady-  
1159 state invadopodia in MTLn3 cells when a Y1105/1087 phosphorylation-deficient mutant  
1160 version of p190RhoGAP was overexpressed. Results are normalized to the Ctrl where  
1161 only the fluorescent protein was overexpressed. Student's t-test, two-tail analysis: \*\*  
1162 p=0.1475; n=3 experiments, shown with SEM.

1163 **Figure 6: TC10 is required for cancer cell metastasis *in vivo***

1164 **a.** The percentage of invading cells in an *in vitro* invasion assay for MTLn3 cells  
1165 transfected with Ctrl or TC10 siRNA. Student's t-test, one-tail pair-wise analysis, \*  
1166 p=0.03928, n=6 experiments. Error bars represent the SEM. **b.** The percentage of  
1167 invading cells in the *in vitro* invasion assay using MTLn3 cells transfected with Ctrl or  
1168 p190RhoGAP siRNA. Student's t-test, two-tail analysis: \* p=0.02495; n=3 experiments;  
1169 shown with SEM. **c.** CRISPR/cas9 knockout populations of TC10 using 4 different  
1170 sgRNA designs. Full-sized western blots are shown in Supplementary Figure S13. **d.**  
1171 The matrix degradation by a TC10 knockout MTLn3 cell population using sgRNA4.

1172 Results are normalized to the NT Ctrl degradation. Student's t-test, one-tail pair-wise  
1173 analysis, \* p=0.03370, n=4 experiments. Error bars represent the SEM. **e**. Functional  
1174 rescue of matrix degradation by the overexpression of WT TC10 in TC10-KO MTLn3  
1175 cells. Results are normalized to the NT Ctrl degradation. Student's t-test, one-tail pair-  
1176 wise analysis, "ns" p=0.1737, n=3 experiments. Error bars represent the SEM. **f**. The  
1177 number of steady-state invadopodia per cell in MTLn3 cells, with or without TC10  
1178 CRISPR/cas9 knockout. Results are normalized to the NT Ctrl. Student's t-test, two-tail  
1179 pair-wise analysis, "ns" p=0.9438, n=4 experiments. Error bars represent the SEM. **g**.  
1180 The lung surface metastases of the Ctrl non-targeting or sgRNA4-TC10 knockout  
1181 MTLn3 cells in the spontaneous metastasis assay, as measured by the stable co-  
1182 transduction of EGFP (insets show representative fields of views). Results are  
1183 normalized to the NT Ctrl. White bars, 100  $\mu$ m. N = 12 mice for Ctr and n = 10 for TC10  
1184 KO. \*\*p =0.001380 (Mann-Whitney U test, two-tail analysis). Error bars represent the  
1185 SEM. **h**. A schematic model showing the pathways regulated through TC10 modulation  
1186 that might impact breast cancer invasion and metastasis.

1187 **References**

1188 1 Itoh, Y. MT1-MMP: a key regulator of cell migration in tissue. *IUBMB Life* **58**, 589-596,  
1189 doi:10.1080/15216540600962818 (2006).

1190 2 Yamaguchi, H. Pathological roles of invadopodia in cancer invasion and metastasis. *Eur  
1191 J Cell Biol* **91**, 902-907, doi:10.1016/j.ejcb.2012.04.005 (2012).

1192 3 Jiang, W. G. *et al.* Expression of membrane type-1 matrix metalloproteinase, MT1-MMP  
1193 in human breast cancer and its impact on invasiveness of breast cancer cells. *Int J Mol  
1194 Med* **17**, 583-590 (2006).

1195 4 Szabova, L., Chrysovergis, K., Yamada, S. S. & Holmbeck, K. MT1-MMP is required for  
1196 efficient tumor dissemination in experimental metastatic disease. *Oncogene* **27**, 3274-  
1197 3281, doi:10.1038/sj.onc.1210982 (2008).

1198 5 Linder, S. MT1-MMP: Endosomal delivery drives breast cancer metastasis. *J Cell Biol*  
1199 **211**, 215-217, doi:10.1083/jcb.201510009 (2015).

1200 6 Paterson, E. K. & Courtneidge, S. A. Invadosomes are coming: new insights into  
1201 function and disease relevance. *FEBS J* **285**, 8-27, doi:10.1111/febs.14123 (2018).

1202 7 Eddy, R. J., Weidmann, M. D., Sharma, V. P. & Condeelis, J. S. Tumor Cell  
1203 Invadopodia: Invasive Protrusions that Orchestrate Metastasis. *Trends Cell Biol*,  
1204 doi:10.1016/j.tcb.2017.03.003 (2017).

1205 8 Meirson, T. & Gil-Henn, H. Targeting invadopodia for blocking breast cancer metastasis.  
1206 *Drug resistance updates : reviews and commentaries in antimicrobial and anticancer  
1207 chemotherapy* **39**, 1-17, doi:10.1016/j.drup.2018.05.002 (2018).

1208 9 Coussens, L. M., Fingleton, B. & Matrisian, L. M. Matrix metalloproteinase inhibitors and  
1209 cancer: trials and tribulations. *Science* **295**, 2387-2392, doi:10.1126/science.1067100  
1210 (2002).

1211 10 Fingleton, B. MMPs as therapeutic targets--still a viable option? *Semin Cell Dev Biol* **19**,  
1212 61-68, doi:10.1016/j.semcd.2007.06.006 (2008).

1213 11 Narumiya, S., Tanji, M. & Ishizaki, T. Rho signaling, ROCK and mDia1, in  
1214 transformation, metastasis and invasion. *Cancer Metastasis Rev* **28**, 65-76 (2009).

1215 12 Yamaguchi, H. *et al.* Molecular mechanisms of invadopodium formation: the role of the  
1216 N-WASP-Arp2/3 complex pathway and cofilin. *J Cell Biol* **168**, 441-452,  
1217 doi:10.1083/jcb.200407076 (2005).

1218 13 Sabeh, F., Li, X. Y., Saunders, T. L., Rowe, R. G. & Weiss, S. J. Secreted versus  
1219 membrane-anchored collagenases: relative roles in fibroblast-dependent collagenolysis  
1220 and invasion. *J Biol Chem* **284**, 23001-23011, doi:10.1074/jbc.M109.002808 (2009).

1221 14 Wisdom, K. M. *et al.* Matrix mechanical plasticity regulates cancer cell migration through  
1222 confining microenvironments. *Nature communications* **9**, 4144, doi:10.1038/s41467-018-  
1223 06641-z (2018).

1224 15 Vega, F. M. & Ridley, A. J. SnapShot: Rho family GTPases. *Cell* **129**, 1430 (2007).

1225 16 Murphy, G. A. *et al.* Cellular functions of TC10, a Rho family GTPase: regulation of  
1226 morphology, signal transduction and cell growth. *Oncogene* **18**, 3831-3845,  
1227 doi:10.1038/sj.onc.1202758 (1999).

1228 17 Murphy, G. A. *et al.* Signaling mediated by the closely related mammalian Rho family  
1229 GTPases TC10 and Cdc42 suggests distinct functional pathways. *Cell Growth Differ* **12**,  
1230 157-167 (2001).

1231 18 Zhang, J. *et al.* Down-regulation of microRNA-9 leads to activation of IL-6/Jak/STAT3  
1232 pathway through directly targeting IL-6 in HeLa cell. *Mol Carcinog* **55**, 732-742,  
1233 doi:10.1002/mc.22317 (2016).

1234 19 Han, S. W. *et al.* RNA editing in RHOQ promotes invasion potential in colorectal cancer.  
1235 *J Exp Med* **211**, 613-621, doi:10.1084/jem.20132209 (2014).

1236 20 Chiang, S. H. *et al.* Insulin-stimulated GLUT4 translocation requires the CAP-dependent  
1237 activation of TC10. *Nature* **410**, 944-948, doi:10.1038/35073608 (2001).

1238 21 Goicoechea, S. M., Awadia, S. & Garcia-Mata, R. I'm coming to GEF you: Regulation of  
1239 RhoGEFs during cell migration. *Cell Adh Migr* **8** (2014).

1240 22 Cherfils, J. & Zeghouf, M. Regulation of small GTPases by GEFs, GAPs, and GDIs.  
1241 *Physiol Rev* **93**, 269-309, doi:10.1152/physrev.00003.2012 (2013).

1242 23 Kawase, K. *et al.* GTP hydrolysis by the Rho family GTPase TC10 promotes exocytic  
1243 vesicle fusion. *Dev Cell* **11**, 411-421, doi:10.1016/j.devcel.2006.07.008 (2006).

1244 24 Hsu, S. C., TerBush, D., Abraham, M. & Guo, W. The exocyst complex in polarized  
1245 exocytosis. *Int Rev Cytol* **233**, 243-265, doi:10.1016/S0074-7696(04)33006-8 (2004).

1246 25 Munson, M. & Novick, P. The exocyst defrocked, a framework of rods revealed. *Nat*  
1247 *Struct Mol Biol* **13**, 577-581, doi:10.1038/nsmb1097 (2006).

1248 26 Dupraz, S. *et al.* The TC10-Exo70 complex is essential for membrane expansion and  
1249 axonal specification in developing neurons. *J Neurosci* **29**, 13292-13301,  
1250 doi:10.1523/JNEUROSCI.3907-09.2009 (2009).

1251 27 Monteiro, P. *et al.* Endosomal WASH and exocyst complexes control exocytosis of MT1-  
1252 MMP at invadopodia. *J Cell Biol* **203**, 1063-1079, doi:10.1083/jcb.201306162 (2013).

1253 28 Kanzaki, M. & Pessin, J. E. Caveolin-associated filamentous actin (Cav-actin) defines a  
1254 novel F-actin structure in adipocytes. *J Biol Chem* **277**, 25867-25869,  
1255 doi:10.1074/jbc.C200292200 (2002).

1256 29 Bogan, J. S. Regulation of glucose transporter translocation in health and diabetes.  
1257 *Annu Rev Biochem* **81**, 507-532, doi:10.1146/annurev-biochem-060109-094246 (2012).

1258 30 Beaty, B. T. *et al.* beta1 integrin regulates Arg to promote invadopodial maturation and  
1259 matrix degradation. *Mol Biol Cell* **24**, 1661-1675, S1661-1611, doi:10.1091/mbc.E12-12-  
1260 0908 (2013).

1261 31 Bravo-Cordero, J. J., Magalhaes, M. A., Eddy, R. J., Hodgson, L. & Condeelis, J.  
1262 Functions of cofilin in cell locomotion and invasion. *Nat Rev Mol Cell Biol* **14**, 405-417,  
1263 doi:10.1038/nrm3609 (2013).

1264 32 Hoshino, D. *et al.* Exosome secretion is enhanced by invadopodia and drives invasive  
1265 behavior. *Cell reports* **5**, 1159-1168, doi:10.1016/j.celrep.2013.10.050 (2013).

1266 33 Liu, J., Yue, P., Artym, V. V., Mueller, S. C. & Guo, W. The role of the exocyst in matrix  
1267 metalloproteinase secretion and actin dynamics during tumor cell invadopodia formation.  
1268 *Mol Biol Cell* **20**, 3763-3771, doi:10.1091/mbc.E08-09-0967 (2009).

1269 34 Inoue, M., Chang, L., Hwang, J., Chiang, S. H. & Saltiel, A. R. The exocyst complex is  
1270 required for targeting of Glut4 to the plasma membrane by insulin. *Nature* **422**, 629-633,  
1271 doi:10.1038/nature01533 (2003).

1272 35 Wu, M., Wu, Z. F., Rosenthal, D. T., Rhee, E. M. & Merajver, S. D. Characterization of  
1273 the roles of RHOC and RHOA GTPases in invasion, motility, and matrix adhesion in  
1274 inflammatory and aggressive breast cancers. *Cancer* **116**, 2768-2782,  
1275 doi:10.1002/cncr.25181 (2010).

1276 36 Ory, S. & Gasman, S. Rho GTPases and exocytosis: what are the molecular links?  
1277 *Semin Cell Dev Biol* **22**, 27-32, doi:10.1016/j.semcdb.2010.12.002 (2011).

1278 37 Johnson, D. I. Cdc42: An essential Rho-type GTPase controlling eukaryotic cell polarity.  
1279 *Microbiol Mol Biol Rev* **63**, 54-105 (1999).

1280 38 Donnelly, S. K. *et al.* Rac3 regulates breast cancer invasion and metastasis by  
1281 controlling adhesion and matrix degradation. *J Cell Biol* **216**, 4331-4349,  
1282 doi:10.1083/jcb.201704048 (2017).

1283 39 Bravo-Cordero, J. J. *et al.* A Novel Spatiotemporal RhoC Activation Pathway Locally  
1284 Regulates Cofilin Activity at Invadopodia. *Curr Biol* **21**, 635-644, doi:S0960-  
1285 9822(11)00311-3 [pii]  
1286 10.1016/j.cub.2011.03.039 (2011).

1287 40 Miskolci, V., Wu, B., Moshfegh, Y., Cox, D. & Hodgson, L. Optical Tools To Study the  
1288 Isoform-Specific Roles of Small GTPases in Immune Cells. *J Immunol* **196**, 3479-3493,  
1289 doi:10.4049/jimmunol.1501655 (2016).

1290 41 Moshfegh, Y., Bravo-Cordero, J. J., Miskolci, V., Condeelis, J. & Hodgson, L. A Trio-  
1291 Rac1-Pak1 signalling axis drives invadopodia disassembly. *Nat Cell Biol* **16**, 574-586,  
1292 doi:10.1038/ncb2972 (2014).

1293 42 Hanna, S., Miskolci, V., Cox, D. & Hodgson, L. A New Genetically Encoded Single-Chain  
1294 Biosensor for Cdc42 Based on FRET, Useful for Live-Cell Imaging. *PLoS One* **9**,  
1295 e96469, doi:10.1371/journal.pone.0096469 (2014).

1296 43 Wu, B., Chen, J. & Singer, R. H. Background free imaging of single mRNAs in live cells  
1297 using split fluorescent proteins. *Scientific reports* **4**, 3615, doi:10.1038/srep03615 (2014).

1298 44 Bravo-Cordero, J. J., Moshfegh, Y., Condeelis, J. & Hodgson, L. Live Cell Imaging of  
1299 RhoGTPase Biosensors in Tumor Cells. *Methods Mol Biol* **1046**, 359-370,  
1300 doi:10.1007/978-1-62703-538-5\_22 (2013).

1301 45 Machacek, M. *et al.* Coordination of Rho GTPase activities during cell protrusion. *Nature*  
1302 **461**, 99-103 (2009).

1303 46 Hodgson, L. *et al.* FRET binding antenna reports spatiotemporal dynamics of GDI-Cdc42  
1304 GTPase interactions. *Nature chemical biology* **12**, 802-809, doi:10.1038/nchembio.2145  
1305 (2016).

1306 47 Arthur, W. T. & Burridge, K. RhoA inactivation by p190RhoGAP regulates cell spreading  
1307 and migration by promoting membrane protrusion and polarity. *Mol Biol Cell* **12**, 2711-  
1308 2720, doi:10.1091/mbc.12.9.2711 (2001).

1309 48 Bidaud-Meynard, A., Biname, F., Lagree, V. & Moreau, V. Regulation of Rho GTPase  
1310 activity at the leading edge of migrating cells by p190RhoGAP. *Small GTPases*, 1-12,  
1311 doi:10.1080/21541248.2017.1280584 (2017).

1312 49 Fujita, A. *et al.* GTP hydrolysis of TC10 promotes neurite outgrowth through exocytic  
1313 fusion of Rab11- and L1-containing vesicles by releasing exocyst component Exo70.  
1314 *PLoS One* **8**, e79689, doi:10.1371/journal.pone.0079689 (2013).

1315 50 Nakahara, H. *et al.* Activation of beta1 integrin signaling stimulates tyrosine  
1316 phosphorylation of p190RhoGAP and membrane-protrusive activities at invadopodia. *J  
1317 Biol Chem* **273**, 9-12, doi:10.1074/jbc.273.1.9 (1998).

1318 51 Bravo-Cordero, J. J. *et al.* Spatial regulation of RhoC activity defines protrusion  
1319 formation in migrating cells. *J Cell Sci* **126**, 3356-3369, doi:10.1242/jcs.123547 (2013).

1320 52 Wu, Y. I. *et al.* A genetically encoded photoactivatable Rac controls the motility of living  
1321 cells. *Nature* **461**, 104-108, doi:nature08241 [pii]  
1322 10.1038/nature08241 (2009).

1323 53 Bradley, W. D., Hernandez, S. E., Settleman, J. & Koleske, A. J. Integrin signaling  
1324 through Arg activates p190RhoGAP by promoting its binding to p120RasGAP and  
1325 recruitment to the membrane. *Mol Biol Cell* **17**, 4827-4836, doi:10.1091/mbc.e06-02-  
1326 0132 (2006).

1327 54 Tomar, A., Lim, S. T., Lim, Y. & Schlaepfer, D. D. A FAK-p120RasGAP-p190RhoGAP  
1328 complex regulates polarity in migrating cells. *J Cell Sci* **122**, 1852-1862,  
1329 doi:10.1242/jcs.046870 (2009).

1330 55 Mader, C. C. *et al.* An EGFR-Src-Arg-cortactin pathway mediates functional maturation  
1331 of invadopodia and breast cancer cell invasion. *Cancer Res* **71**, 1730-1741,  
1332 doi:10.1158/0008-5472.CAN-10-1432 (2011).

1333 56 Razidlo, G. L., Schroeder, B., Chen, J., Billadeau, D. D. & McNiven, M. A. Vav1 as a  
1334 central regulator of invadopodia assembly. *Curr Biol* **24**, 86-93,  
1335 doi:10.1016/j.cub.2013.11.013 (2014).  
1336 57 Liu, B. P. & Burridge, K. Vav2 activates Rac1, Cdc42, and RhoA downstream from  
1337 growth factor receptors but not beta1 integrins. *Mol Cell Biol* **20**, 7160-7169 (2000).  
1338 58 Settleman, J., Albright, C. F., Foster, L. C. & Weinberg, R. A. Association between  
1339 GTPase activators for Rho and Ras families. *Nature* **359**, 153-154,  
1340 doi:10.1038/359153a0 (1992).  
1341 59 Muller, P. M. et al. Systems analysis of RhoGEF and RhoGAP regulatory proteins  
1342 reveals spatially organized RAC1 signalling from integrin adhesions. *Nat Cell Biol* **22**,  
1343 498-511, doi:10.1038/s41556-020-0488-x (2020).  
1344 60 Marchesin, V. et al. ARF6-JIP3/4 regulate endosomal tubules for MT1-MMP exocytosis  
1345 in cancer invasion. *J Cell Biol* **211**, 339-358, doi:10.1083/jcb.201506002 (2015).  
1346 61 Hu, K. Q. & Settleman, J. Tandem SH2 binding sites mediate the RasGAP-RhoGAP  
1347 interaction: a conformational mechanism for SH3 domain regulation. *EMBO J* **16**, 473-  
1348 483, doi:10.1093/emboj/16.3.473 (1997).  
1349 62 Warren, M. S. et al. Integrin beta1 signals through Arg to regulate postnatal dendritic  
1350 arborization, synapse density, and behavior. *J Neurosci* **32**, 2824-2834,  
1351 doi:10.1523/JNEUROSCI.3942-11.2012 (2012).  
1352 63 Simpson, M. A. et al. Direct interactions with the integrin beta1 cytoplasmic tail activate  
1353 the Abl2/Arg kinase. *J Biol Chem* **290**, 8360-8372, doi:10.1074/jbc.M115.638874 (2015).  
1354 64 Oser, M. et al. Cortactin regulates cofilin and N-WASp activities to control the stages of  
1355 invadopodium assembly and maturation. *J Cell Biol* **186**, 571-587,  
1356 doi:10.1083/jcb.200812176 (2009).  
1357 65 Mai, A. et al. Competitive binding of Rab21 and p120RasGAP to integrins regulates  
1358 receptor traffic and migration. *J Cell Biol* **194**, 291-306, doi:10.1083/jcb.201012126  
1359 (2011).  
1360 66 Neri, A. & Nicolson, G. L. Phenotypic drift of metastatic and cell-surface properties of  
1361 mammary adenocarcinoma cell clones during growth in vitro. *Int J Cancer* **28**, 731-738  
1362 (1981).  
1363 67 Segall, J. E. et al. EGF stimulates lamellipod extension in metastatic mammary  
1364 adenocarcinoma cells by an actin-dependent mechanism. *Clin.Exp.Metast.* **14**, 61-72  
1365 (1996).  
1366 68 Courtneidge, S. A., Azucena, E. F., Pass, I., Seals, D. F. & Tesfay, L. The SRC  
1367 substrate Tks5, podosomes (invadopodia), and cancer cell invasion. *Cold Spring Harb  
1368 Symp Quant Biol* **70**, 167-171, doi:10.1101/sqb.2005.70.014 (2005).  
1369 69 Ehrhardt, C. et al. Polyethylenimine, a cost-effective transfection reagent. *Signal  
1370 Transduction* **6**, 179-184, doi:10.1002/sita.200500073 (2006).  
1371 70 Benard, V. & Bokoch, G. M. Assay of Cdc42, Rac, and Rho GTPase activation by affinity  
1372 methods. *Methods Enzymol* **345**, 349-359 (2002).  
1373 71 Shalem, O. et al. Genome-scale CRISPR-Cas9 knockout screening in human cells.  
1374 *Science* **343**, 84-87, doi:10.1126/science.1247005 (2014).  
1375 72 Sanjana, N. E., Shalem, O. & Zhang, F. Improved vectors and genome-wide libraries for  
1376 CRISPR screening. *Nat Methods* **11**, 783-784, doi:10.1038/nmeth.3047 (2014).  
1377 73 Shcherbakova, D. M. et al. Bright monomeric near-infrared fluorescent proteins as tags  
1378 and biosensors for multiscale imaging. *Nature communications* **7**, 12405,  
1379 doi:10.1038/ncomms12405 (2016).  
1380 74 Bravo-Cordero, J. J. et al. MT1-MMP proinvasive activity is regulated by a novel Rab8-  
1381 dependent exocytic pathway. *Embo J* **26**, 1499-1510, doi:10.1038/sj.emboj.7601606  
1382 (2007).

1383 75 Bindels, D. S. *et al.* mScarlet: a bright monomeric red fluorescent protein for cellular  
1384 imaging. *Nat Methods* **14**, 53-56, doi:10.1038/nmeth.4074 (2017).  
1385 76 Subach, O. M., Cranfill, P. J., Davidson, M. W. & Verkhusha, V. V. An enhanced  
1386 monomeric blue fluorescent protein with the high chemical stability of the chromophore.  
1387 *PLoS One* **6**, e28674, doi:10.1371/journal.pone.0028674 (2011).  
1388 77 Wu, B. *et al.* Synonymous modification results in high-fidelity gene expression of  
1389 repetitive protein and nucleotide sequences. *Genes Dev* **29**, 876-886,  
1390 doi:10.1101/gad.259358.115 (2015).  
1391 78 Nalbant, P., Hodgson, L., Kraynov, V., Touthkine, A. & Hahn, K. M. Activation of  
1392 endogenous Cdc42 visualized in living cells. *Science* **305**, 1615-1619 (2004).  
1393 79 Spiering, D. & Hodgson, L. Multiplex Imaging of Rho Family GTPase Activities in Living  
1394 Cells. *Methods Mol Biol* **827**, 215-234, doi:10.1007/978-1-61779-442-1\_15 (2012).  
1395 80 Spiering, D., Bravo-Cordero, J. J., Moshfegh, Y., Miskolci, V. & Hodgson, L. Quantitative  
1396 Ratiometric Imaging of FRET-Biosensors in Living Cells. *Methods Cell Biol* **114**, 593-  
1397 609, doi:10.1016/B978-0-12-407761-4.00025-7 (2013).  
1398 81 Pertz, O. & Hahn, K. M. Designing biosensors for Rho family proteins--deciphering the  
1399 dynamics of Rho family GTPase activation in living cells. *J Cell Sci* **117**, 1313-1318,  
1400 doi:10.1242/jcs.01117 (2004).  
1401 82 Hodgson, L., Pertz, O. & Hahn, K. M. Design and optimization of genetically encoded  
1402 fluorescent biosensors: GTPase biosensors. *Methods Cell Biol* **85**, 63-81 (2008).  
1403 83 Efron, B. & Tibshirani, R. *An Introduction to the bootstrap*. Vol. xvi (Chapman & Hall,  
1404 1993).  
1405 84 Zhou, Z. N. *et al.* Autocrine HBEGF expression promotes breast cancer intravasation,  
1406 metastasis and macrophage-independent invasion in vivo. *Oncogene* **33**, 3784-3793,  
1407 doi:10.1038/onc.2013.363 (2014).  
1408 85 Shcherbakova, D. M., Cox Cammer, N., Huisman, T. M., Verkhusha, V. V. & Hodgson,  
1409 L. Direct multiplex imaging and optogenetics of Rho GTPases enabled by near-infrared  
1410 FRET. *Nature chemical biology*, doi:10.1038/s41589-018-0044-1 (2018).  
1411

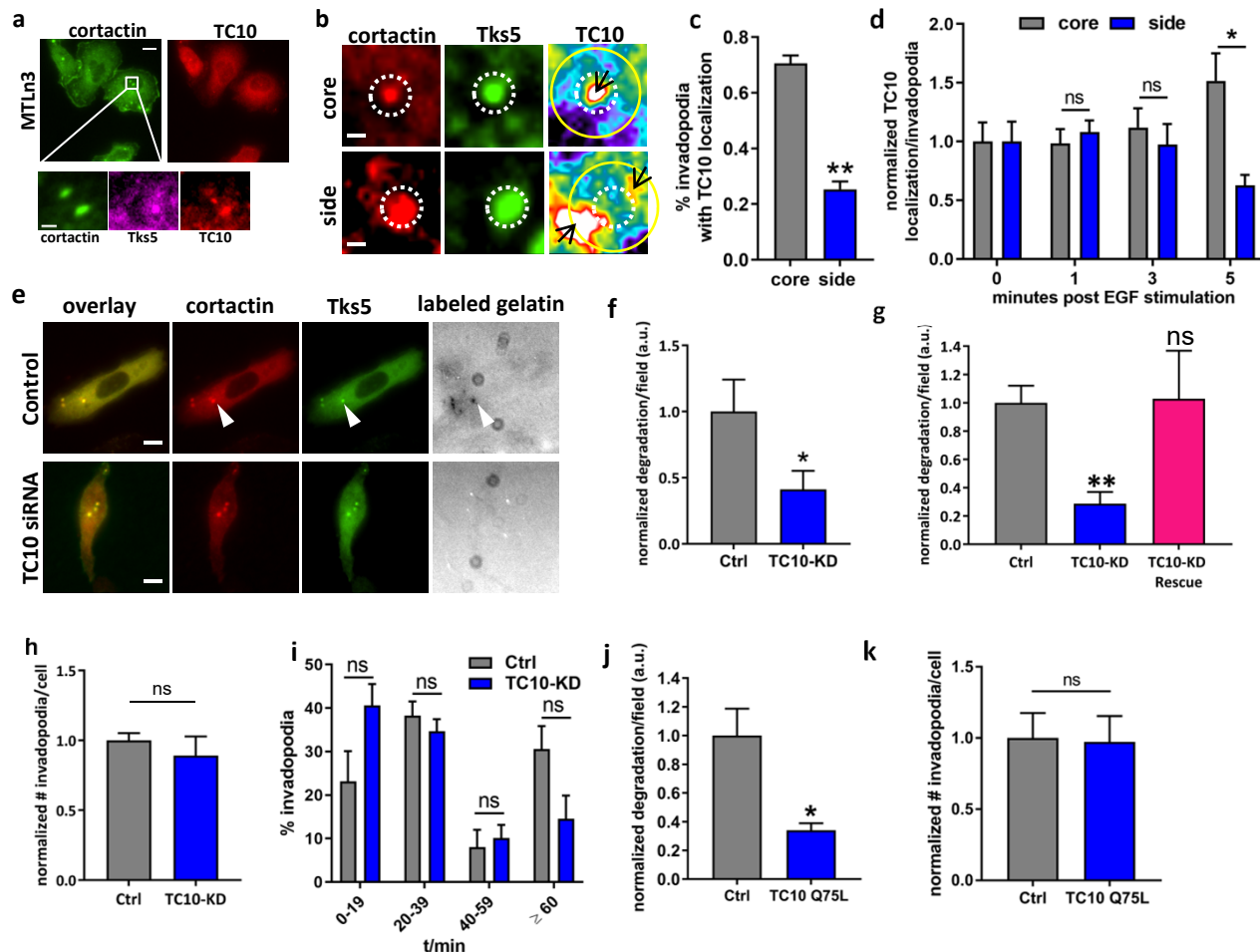


**Figure 1: TC10 is localized at invadopodia and required for matrix degradation.**

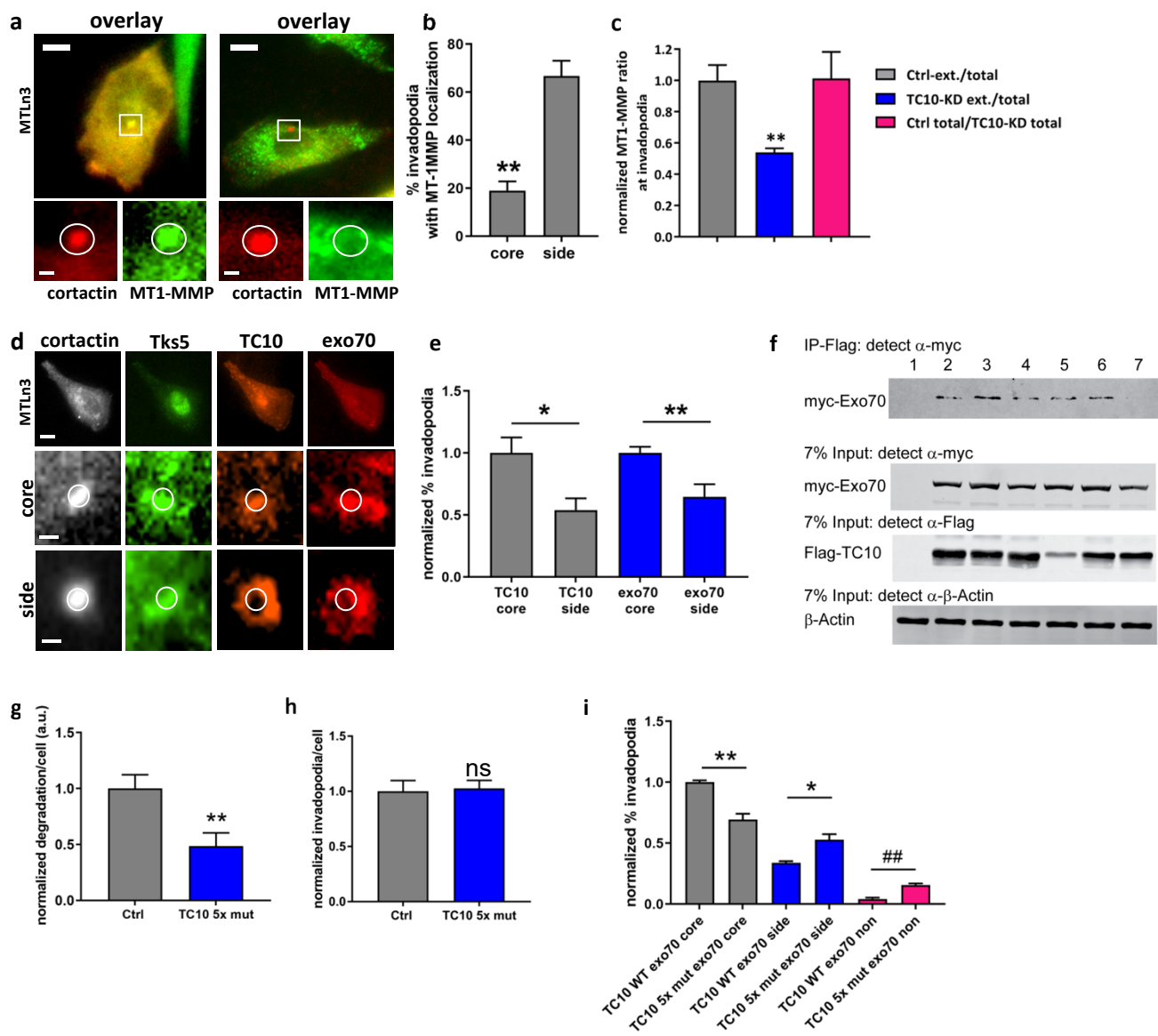


**Figure 2: TC10 regulates MT1-MMP exposure at the plasma membrane of invadopodia.**

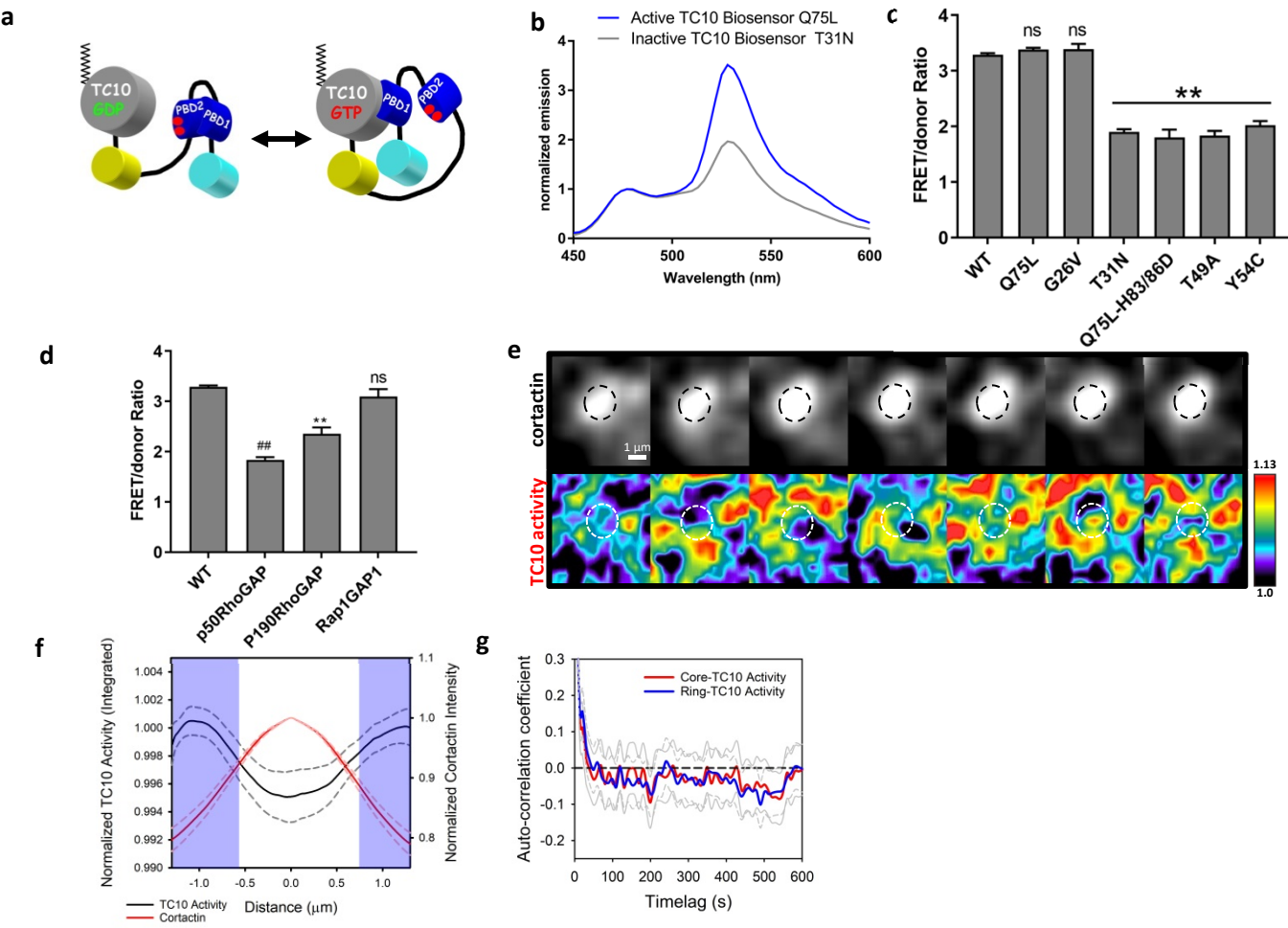


**Figure 3: TC10 activity at invadopodia is spatially regulated.**

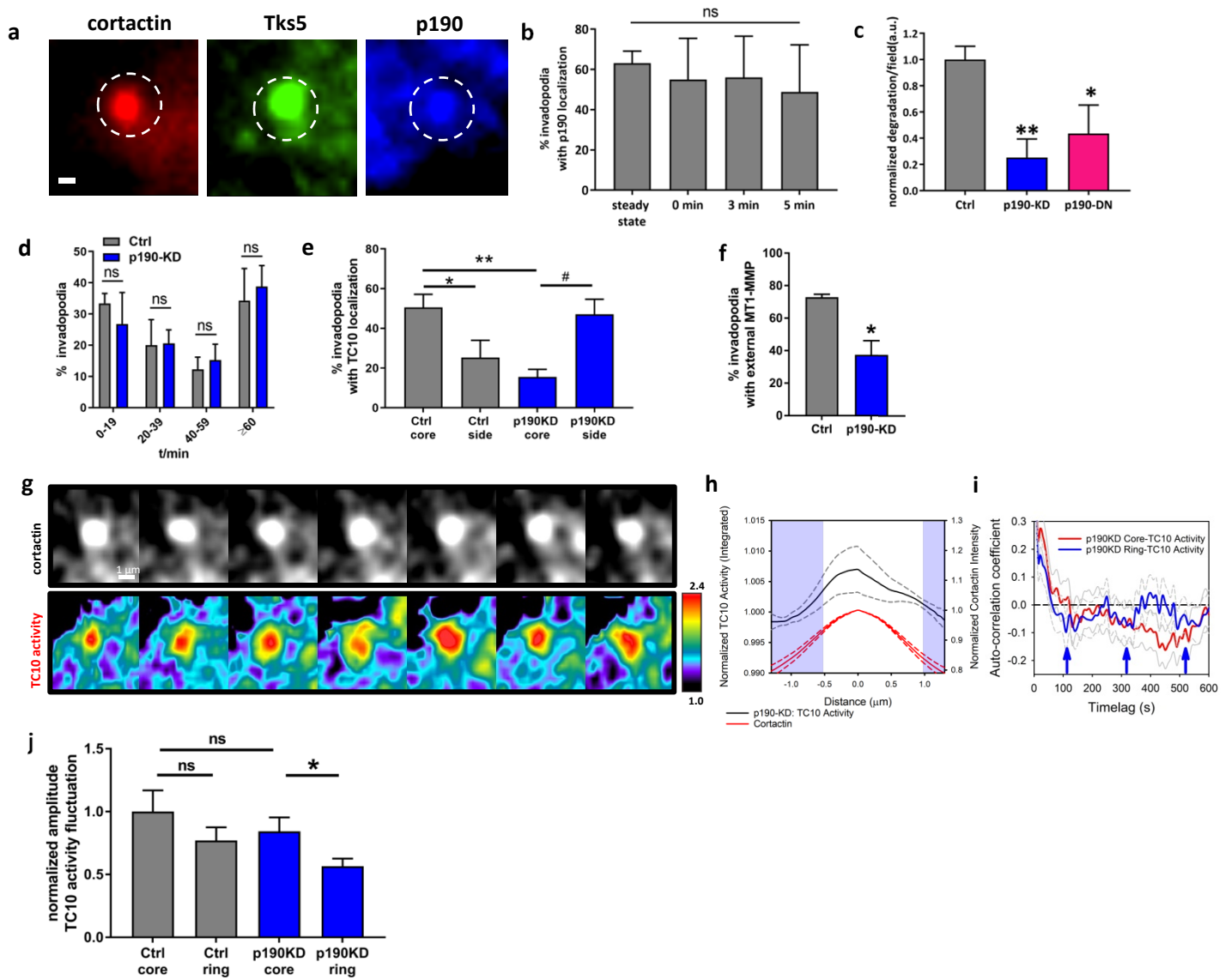


**Figure 4: p190RhoGAP impacts invadopodia function by targeting TC10.**

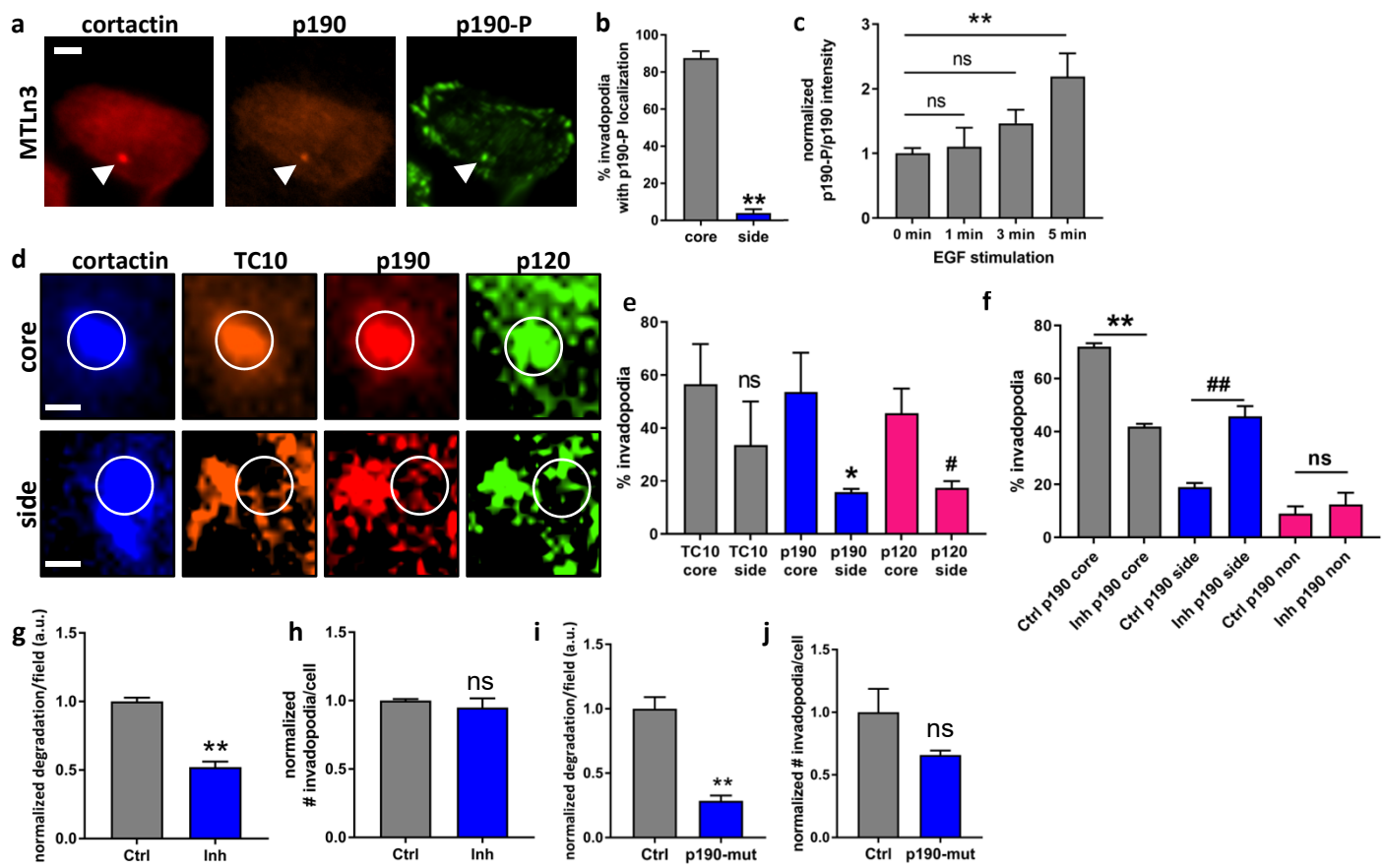


**Figure 5: The tyrosine phosphorylation of p190RhoGAP is required for matrix degradation**

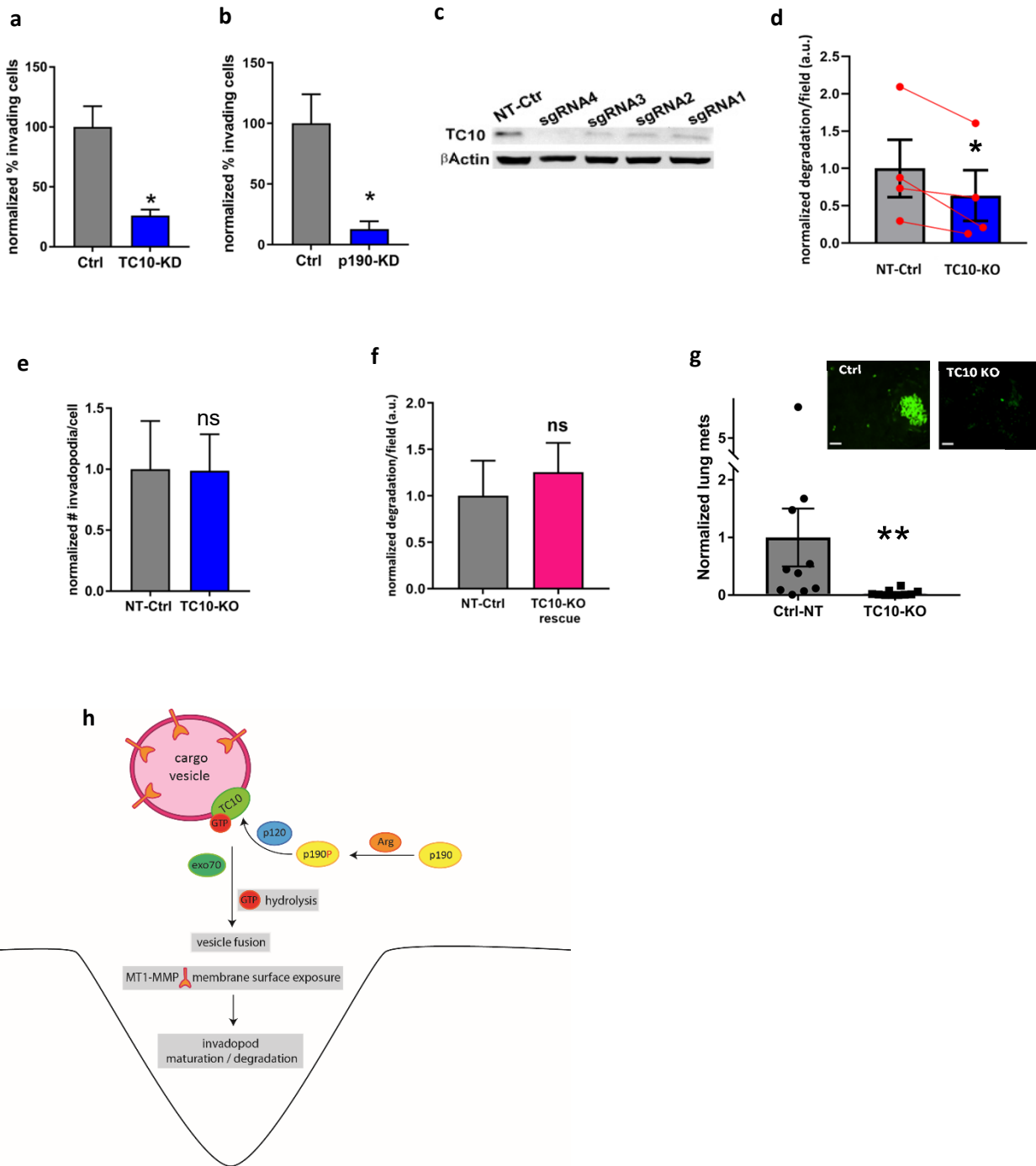


**Figure 6: TC10 is required for cancer cell metastasis in vivo**